Fermilab FERMILAB-Pub-01/413-A October 2002

Composite Quasar Spectra From the Sloan Digital Sky Survey[1]

Daniel E. Vanden Berk[2], Gordon T. Richards[3], Amanda Bauer[4], Michael A. Strauss[5], Donald P. Schneider[3], Timothy M. Heckman[6], Donald G. York[7,8], Patrick B. Hall[5], Xiaohui Fan[5,9], G. R. Knapp[5], Scott F. Anderson[10], James Annis[2], Neta A. Bahcall[5], Mariangela Bernardi[7], John W. Briggs[7], J. Brinkmann[11], Robert Brunner[12], Scott Burles[2], Larry Carey[10], Francisco J. Castander[7,13], A. J. Connolly[14], J. H. Crocker[6], István Csabai[6,15], Mamoru Doi[16], Douglas Finkbeiner[17], Scott Friedman[6], Joshua A. Frieman[2,7], Masataka Fukugita[18], James E. Gunn[5], G. S. Hennessy[19], Željko Ivezić[5], Stephen Kent[2,7], Peter Z. Kunszt[6], D.Q. Lamb[7], R. French Leger[10], Daniel C. Long[11], Jon Loveday[20], Robert H. Lupton[5], Avery Meiksin[21], Aronne Merelli[12,22], Jeffrey A. Munn[23], Heidi Jo Newberg[24], Matt Newcomb[22], R. C. Nichol[22], Russell Owen[10], Jeffrey R. Pier[23], Adrian Pope[6,22], Constance M. Rockosi[7], David J. Schlegel[5], Walter A. Siegmund[10], Stephen Smee[6,25], Yehuda Snir[22], Chris Stoughton[2], Christopher Stubbs[10], Mark SubbaRao[7], Alexander S. Szalay[6], Gyula P. Szokoly[6], Christy Tremonti[6], Alan Uomoto[6], Patrick Waddell[10], Brian Yanny[2], Wei Zheng[6]

ABSTRACT

We have created a variety of composite quasar spectra using a homogeneous data set of over 2200 spectra from the Sloan Digital Sky Survey (SDSS). The quasar sample spans a redshift range of $0.044 \leq z \leq 4.789$, and an absolute r' magnitude range of -18.0 to -26.5. The input spectra cover an observed wavelength range of $3800 - 9200$Å

---

[1]Based on observations obtained with the Sloan Digital Sky Survey, which is owned and operated by the Astrophysical Research Consortium.

[2]Fermi National Accelerator Laboratory, P.O. Box 500, Batavia, IL 60510

[3]Department of Astronomy and Astrophysics, The Pennsylvania State University, University Park, PA 16802

[4]Department of Physics, University of Cincinnati, 400 Physics Bldg., Cincinnati, OH 45221

[5]Princeton University Observatory, Princeton, NJ 08544

[6]Department of Physics and Astronomy, The Johns Hopkins University, 3701 San Martin Drive, Baltimore, MD 21218

[7]The University of Chicago, Department of Astronomy and Astrophysics, 5640 S. Ellis Ave., Chicago, IL 60637

[8]The University of Chicago, Enrico Fermi Institute, 5640 S. Ellis Ave., Chicago, IL 60637

[9]Institute for Advanced Study, Olden Lane, Princeton, NJ 08540

[10]University of Washington, Department of Astronomy, Box 351580, Seattle, WA 98195

[11]Apache Point Observatory, P.O. Box 59, Sunspot, NM 88349-0059

[12]Department of Astronomy, California Institute of Technology, Pasadena, CA 91125

[13]Observatoire Midi Pyrenees, 14 ave Edouard Belin, Toulouse, F-31400, France

[14]Department of Physics and Astronomy, University of Pittsburgh, Pittsburgh, PA 15260

[15]Department of Physics of Complex Systems, Eötvös University, Pázmány Péter sétány 1

[16]Department of Astronomy and Research Center for the Early Universe, School of Science, University of Tokyo, Hongo, Bunkyo, Tokyo, 113-0033, Japan

[17]University of California at Berkeley, Departments of Physics and Astronomy, 601 Campbell Hall, Berkeley, CA 94720

[18]University of Tokyo, Institute for Cosmic Ray Reserach, Kashiwa, 2778582, Japan

[19]U.S. Naval Observatory, 3450 Massachusetts Ave., NW, Washington, DC 20392-5420

[20]Astronomy Centre, University of Sussex, Falmer, Brighton BN1 9QJ, United Kingdom

[21]Royal Observatory, Edinburgh, EH9 3HJ, United Kingdom

[22]Dept. of Physics, Carnegie Mellon University, 5000 Forbes Ave., Pittsburgh, PA-15232

[23]U.S. Naval Observatory, Flagstaff Station, P.O. Box 1149, Flagstaff, AZ 86002-1149

[24]Physics Department, Rensselaer Polytechnic Institute, SC1C25, Troy, NY 12180

[25]Department of Astronomy, University of Maryland, College Park, MD 20742-2421

at a resolution of 1800. The median composite covers a rest wavelength range from $800 - 8555\,\text{Å}$, and reaches a peak signal-to-noise ratio of over 300 per 1 Å resolution element in the rest frame. We have identified over 80 emission line features in the spectrum. Emission line shifts relative to nominal laboratory wavelengths are seen for many of the ionic species. Peak shifts of the broad permitted and semi-forbidden lines are strongly correlated with ionization energy, as previously suggested, but we find that the narrow forbidden lines are also shifted by amounts which are strongly correlated with ionization energy. The magnitude of the forbidden line shifts is $\lesssim 100\,\text{km s}^{-1}$, compared to shifts of up to $550\,\text{km s}^{-1}$ for some of the permitted and semi-forbidden lines. At wavelengths longer than the Lyα emission, the continuum of the geometric mean composite is well-fit by two power-laws, with a break at ≈ 5000 Å. The frequency power law index, α_ν, is -0.44 from $\approx 1300 - 5000$ Å, and -2.45 redward of ≈ 5000 Å. The abrupt change in slope can be accounted for partly by host galaxy contamination at low redshift. Stellar absorption lines, including higher-order Balmer lines, seen in the composites suggest that young or intermediate age stars make a significant contribution to the light of the host galaxies. Most of the spectrum is populated by blended emission lines, especially in the range $1500 - 3500$ Å, which can make the estimation of quasar continua highly uncertain unless large ranges in wavelength are observed. An electronic table of the median quasar template is available.

Subject headings: quasars: emission lines — quasars:general

1. Introduction

Most quasar spectra from ultraviolet to optical wavelengths can be characterized by a featureless continuum and a series of mostly broad emission line features; compared with galaxies or stars, these spectra are remarkably similar from one quasar to another. The first three principal components spectra account for about 75% of the intrinsic quasar variance (Francis, Hewett, Foltz & Chaffee 1992). Subtle global spectral properties can be studied by combining large numbers of quasar spectra into composites. The most detailed composites (Francis et al. 1991; Zheng et al. 1997; Brotherton et al. 2000) use hundreds of moderate resolution spectra, and typically cover a few thousand Å in the quasar rest frame. These high signal-to-noise ratio (S/N) spectra reveal variations from a single power law in the general continuum shape, and weak emission features that are rarely detectable in individual quasar spectra.

The Sloan Digital Sky Survey (York et al. 2000, SDSS) already contains spectra for over 2500 quasars as of June 2000, and by survey end will include on the order of 10^5 quasar spectra. The identification and basic measurement of this sample will be done using an automated pipeline, part of which uses templates for object classification and redshift determination. As one of the first uses of the initial set of spectra, we have created a composite quasar spectrum for use as a

template. The large number of spectra, their wavelength coverage, relatively high resolution, and high signal-to-noise ratio, make the current SDSS sample ideal for the creation of composite quasar spectra. The resulting composite spectrum covers a vacuum rest wavelength range of $800 - 8555$ Å. The peak S/N per 1 Å resolution element is over 300 near 2800Å – several times higher than the previous best ultraviolet/optical composites (e.g. Francis et al. 1991; Zheng et al. 1997; Brotherton et al. 2000).

In addition to serving as a cross-correlation template, the composite is useful for the precise measurement of emission line shifts relative to nominal laboratory wavelengths, calculation of quasar colors for improved candidate selection and photometric redshift estimates, the calculation of K-corrections used in evaluating the quasar luminosity function, and for the estimation of the backlighting flux density continuum for measurements of quasar absorption line systems. Composites can also be made from sub-samples of the input spectra chosen according to quasar properties such as luminosity, redshift, and radio loudness. The dependence of global spectral characteristics on various quasar properties will be the subject of a future paper (Vanden Berk et al. 2001). Here we concentrate on the continuum and emission line properties of the global composite. We describe the SDSS quasar sample in § 2, and the method used to generate the composite spectra in § 3. The continuum and emission line features are measured and discussed in §§ 4 and 5. Wavelengths throughout the paper are vacuum values, except when using the common notation for line identification (truncated air values for wavelengths greater than 3000Å, and truncated vacuum values for wavelengths less than 3000Å). We use the following values for cosmological parameters throughout the paper: $H_0 = 100\,\mathrm{km\,s^{-1}}$, $\Omega_m = 1.0$, $\Omega_\Lambda = 0$, ($q_0 = 0.5$).

2. The SDSS Quasar Sample

The spectra were obtained as part of the commissioning phase of the Sloan Digital Sky Survey. Details of the quasar candidate target selection and spectroscopic data reduction will be given in future papers (Richards et al. 2001b; Newberg et al. 2001; Frieman et al. 2001). The process is summarized here. Quasar candidates are selected in the color space of the SDSS $u'g'r'i'z'$ filter system (Fukugita et al. 1996), from objects found in imaging scans with the SDSS 2.5m telescope and survey camera (Gunn et al. 1998). The effective central wavelengths of the filters for a power-law spectrum with a frequency index of $\alpha = -0.5$, are approximately $3560, 4680, 6175, 7495,$ and 8875Å for $u'g'r'i'z'$ respectively. Quasar candidates are well-separated from the stellar locus in color space, and the filter system allows the discovery of quasars over the full range of redshifts from $z = 0$ to $z \approx 7$. The locations of known quasars in the SDSS color space as a function of redshift are shown by Fan et al. (1999, 2000, 2001); Newberg et al. (1999); Schneider et al. (2001) and especially Richards et al. (2001a) who plot the locations of over 2600 quasars for which there is SDSS photometry. Quasar candidates are selected to $i' \approx 19$ in the low-redshift ($z \lesssim 2.5$) regions of color space, and no discrimination is made against extended objects in those regions. High-redshift quasar candidates are selected to $i' \approx 20$. Objects are also selected as quasar candidates if they

are point sources with $i' \leq 19$ and match objects in the VLA FIRST radio source catalog (Becker, White & Helfand 1995). Thus, quasars in the SDSS are selected both by optical and radio criteria. These data were taken while the hardware, and in particular the target selection software, was being commissioned. Therefore, the selection criteria for quasars has evolved somewhat over the course of these observations, and will not exactly match the final algorithm discussed in Richards et al. (2001b). Because of the changing quasar selection criteria and the loose definition of 'quasar', discretion should be exercised when using the global composite spectra generated from this quasar sample as templates for quasars in other surveys, or subsets of the SDSS quasar sample.

The candidates were observed using the 2.5m SDSS telescope (Siegmund et al. 2001) at Apache Point Observatory, and a pair of double fiber-fed spectrographs (Uomoto et al. 2001). Targeted objects are grouped into 3 degree diameter "plates", each of which holds 640 optical fibers. The fibers subtend $3''$ on the sky and their positions on the plates correspond to the coordinates of candidate objects, sky positions, and calibration stars. Approximately 100 fibers per plate are allocated to quasar candidates. At least three 15 minute exposures are taken per plate. So far, spectra have been taken mainly along a 2.5 degree wide strip centered on the Celestial Equator, with a smaller fraction at other declinations. The spectra in this study were grouped on 66 plates which overlap somewhat to cover approximately 320 square degrees of sky covered by the imaging survey. The plates were observed from October, 1999 to June, 2000. The raw spectra were reduced with the SDSS spectroscopic pipeline (Frieman et al. 2001), which produces wavelength- and flux-calibrated spectra that cover an observed wavelength range from $3800 - 9200$Å at a spectral resolution of approximately 1850 blueward of 6000Å, and 2200 redward of 6000Å. These spectra and more will be made publicly available – in electronic form – in June 2001 as part of the SDSS Early Data Release (Stoughton et al. 2001).

The flux calibration is only approximate at this time, and a point which deserves elaboration since it is the most important source of uncertainty in the continuum shapes of the spectra. Light losses from differential refraction during the observations are minimized by tracking guide stars through a g' filter – the bluest filter within the spectral range. Several F subdwarf stars are selected for observation (simultaneously with the targeted objects) on each plate. One of these – usually the bluest one – is selected, typed, and used to define the response function. This process also largely corrects for Galactic extinction, since the distances to the F subdwarfs employed are typically greater than 2.5kpc, and all of the survey area is at high Galactic latitude. Uncertainties can arise in the spectral typing of the star, and from any variation in response across a plate. A check on the accuracy of the flux calibration is made for each plate by convolving the calibrated spectra with the filter transmission functions of the g', r', and i' bands, and comparing the result to magnitudes derived from the imaging data using an aperture the same diameter as the spectroscopic fibers. For a sample of about 2300 SDSS quasar spectra, the median color difference between the photometric and spectral measurements, after correcting the photometric values for Galactic extinction (Schlegel, Finkbeiner, & Davis 1998), was found to be $\Delta(g' - r') \approx 0.01$ and $\Delta(r' - i') \approx 0.04$. This means that the spectra tend to be slightly bluer than expectations from photometry. For a pure power-law

spectrum with true frequency index of $\alpha_\nu = -0.5$, which is often used to approximate quasars, the difference in both colors would result in a measured index which is systematically greater (bluer) by about 0.1. Quasar spectra are not pure power-laws, and the color differences are well within the intrinsic scatter of quasars at all redshifts (Richards et al. 2001a). Also, the SDSS photometric calibration is not yet finalized, and the shapes of the filter transmission curves are still somewhat uncertain, both of which could contribute to the spectroscopic vs. photometric color differences. The colors of the combined spectra agree well with the color-redshift relationships found by Richards et al. (2001a), (see §§ 4.2,5) which also leads us to believe that the flux calibrations are reasonably good. However, we caution that the results here on the combined continuum shape cannot be considered final until the SDSS spectroscopic calibration is verified.

Quasars were identified from their spectra and approximate redshift measurements were made by manual inspection.[26] We define quasar to mean any extra-galactic object with at least one broad emission line, and that is dominated by a non-stellar continuum. This includes Seyfert galaxies as well as quasars, and we do not make a distinction between them. Spectra were selected if the rest-frame FWHM of the strong permitted lines, such as C IV , Mg II , and the Balmer lines, were greater than about $500\,\mathrm{km\,s^{-1}}$. In most cases those line widths well exceeded $1000\,\mathrm{km\,s^{-1}}$. Since we require only one broad emission line, some objects which may otherwise be classified as "Type 2" AGN (those with predominantly narrow emission lines) are also included in the quasar sample. Spectra with continua dominated by stellar features, such as unambiguous Ca H and K lines, or the 4308Å G-band, were rejected. This definition is free from traditional luminosity or morphology-based criteria, and is also intended to avoid introducing a significant spectral component from the host galaxies (see § 5). Spectra with broad absorption line features (BAL quasars), which comprise about 4% of the initial sample, were removed from the input list. We are studying BAL quasars in the SDSS sample intensively, and initial results are forthcoming (Menou et al. 2001, e.g.); the focus of the present paper is on the intrinsic continua of quasars, and BAL features can heavily obscure the continua. Other spectra with spurious artifacts introduced either during the observations or by the data reduction process (about 10% of the initial sample) were removed from the input list.[27] Spectra obtained as part of SDSS follow-up observations on other telescopes, such as the high-redshift samples of Fan et al. (1999, 2000, 2001), Schneider et al. (2000, 2001), and Zheng et al. (2000) were not included. Figure 1 shows the redshift distribution of the quasars used in the composite, and the absolute r' magnitudes vs. redshift. Discontinuities in the selection function for the quasars, such as the fainter magnitude limit for high-redshift candidates, are evident in Figure 1. The final list of spectra contains 2204 quasars spanning a redshift range of $0.044 \leq z \leq 4.789$, with a median quasar redshift of $\overline{z} = 1.253$. The vast majority of the magnitudes lie in the range $17.5 < r' < 20.5$.

[26] Refined redshift measurements were made later as described in § 3.

[27] These artifacts are due to the inevitable problems of commissioning both the software and hardware, and the problem rate is now negligible.

3. Generating the Composites

The steps required to generate a composite quasar spectrum involve selecting the input spectra, determining accurate redshifts, rebinning the spectra to the rest frame, scaling or normalizing the spectra, and stacking the spectra into the final composite. Each of these steps can have many variations, and their effect on the resulting spectrum can be significant (see Francis et al. (1991) for a discussion of some of these effects). The selection of the input spectra was described in the previous section, and here we detail the remaining steps.

The appropriate statistical methods used to combine the spectra depend upon the spectral quantities of interest. We are interested in both the large-scale continuum shape and the emission line features of the combined quasars. We have used combining techniques to generate two composite spectra: 1) the median spectrum which preserves the relative fluxes of the emission features; and 2) the geometric mean spectrum which preserves the global continuum shape. We have used the geometric mean because quasar continua are often approximated by power-laws, and the median (or arithmetic mean) of a sample of power-law spectra will not in general result in a power-law with the mean index. The geometric mean is defined as, $\langle f_\lambda \rangle_{gm} = (\prod_{i=1}^{n} f_{\lambda,i})^{1/n}$, where $f_{\lambda,i}$ is the flux density of spectrum number i in the bin centered on wavelength λ, and n is the number of spectra contributing to the bin. Assuming a power-law form for the continuum flux density, $f_\lambda \propto \lambda^{-(\alpha_\nu+2)}$, it is easily shown that $\langle f_\lambda \rangle_{gm} \propto \lambda^{-(\langle\alpha_\nu\rangle+2)}$, where $\langle\alpha_\nu\rangle$ is the (arithmetic) mean value of the frequency power-law index. (The wavelength index, α_λ, and the frequency index, α_ν, are related by $\alpha_\lambda = -(\alpha_\nu + 2)$.)

The rest positions of emission lines in quasar spectra, especially the high-ionization broad lines, are known to vary from their nominal laboratory wavelengths (Gaskell 1982; Wilkes 1986; Espey et al. 1989; Zheng & Sulentic 1990; Corbin 1990; Weymann, Morris, Foltz & Hewett 1991; Tytler & Fan 1992; Brotherton, Wills, Steidel & Sargent 1994; Laor et al. 1995; McIntosh, Rix, Rieke & Foltz 1999), so the adopted redshifts of quasars depend upon the lines measured. In addition to understanding the phenomenon of line shifts, unbiased redshifts are important for understanding the nature of associated absorption line systems (Foltz et al. 1986), for accurately measuring the intergalactic medium ionizing flux (Bajtlik, Duncan & Ostriker 1988), and understanding the dynamics of close pairs of quasars. If the redshifts are consistently measured, say using a common emission line or by cross-correlation with a template, then the mean relative line shifts can be measured accurately with a composite made using those redshifts. For the redshifts of our quasars, we have used only the [O III] λ5007 emission line when possible, since it is narrow, bright, unblended, and is presumed to be emitted at nearly the systemic redshift of the host galaxy (Gaskell 1982; Vrtilek & Carleton 1985; McIntosh, Rix, Rieke & Foltz 1999). Some weak Fe II emission is expected near 5000Å (Wills, Netzer & Wills 1985; Verner et al. 1999; Forster et al. 2001, e.g.), but after subtraction of a local continuum (see § 4.2), contamination of the narrow [O III] line by the broad Fe II complex should be less than a few percent at most. Additionally, we use only the top $\approx 50\%$ of the emission line peak to measure its position, which greatly reduces uncertainties due to line asymmetry. An initial composite was made (as described below) using spectra with measured [O III]

emission, and this composite was used as a cross-correlation template for quasars in which the [O III] line was not observable. In this way, all quasars were put onto a common redshift calibration, i.e. relative to the [O III] λ5007 line. We now explain this in detail.

3.1. Generating the [O III] Template

The [O III] based spectrum was made using 373 spectra with a strong [O III] λ5007 emission line unaffected by night sky lines, and includes quasars with redshifts from $z = 0.044$ to $z = 0.840$. Spectra were combined at rest wavelengths which were covered by at least 3 independent spectra, which resulted in a final wavelength coverage of $2070\text{Å} < \lambda < 8555\text{Å}$ for the [O III] based spectrum. The redshifts were based upon the peak position of the [O III] λ5007 line, estimated by calculating the mode of the top $\approx 50\%$ of the line using the relation, mode $= 3 \times$median $- 2 \times$mean, which gives better peak estimates than the centroid or median for slightly skewed profiles (e.g. Lupton 1993). Uncertainties in the peak positions were estimated by taking into account the errors in the flux density of the pixels contributing to the emission line. The mean uncertainty in the peak positions was $35\,\mathrm{km\,s^{-1}}$ (rest frame velocity). This is a few times larger than the wavelength calibration uncertainty of $< 10\,\mathrm{km\,s^{-1}}$, based upon spectral observations of radial velocity standards (York et al. 2000). The wavelength array of each spectrum was shifted to the rest frame using the redshift based on the [O III] line. The wavelengths and flux densities were rebinned onto a common dispersion of 1Å per bin – roughly the resolution of the observed spectra shifted to the rest frame – while conserving flux. Flux values in pixels which overlapped more than one new bin were distributed among the new bins according to the fraction of the original pixel width covering each new bin. The spectra were ordered by redshift and the flux density of the first spectrum was arbitrarily scaled. The other spectra were scaled in order of redshift to the average of the flux density in the common wavelength region of the mean spectrum of all of the lower redshift spectra. The final spectrum was made by finding the median flux density in each bin of the shifted, rebinned, and scaled spectra.

The [O III] based median composite was then used as a template to refine redshift estimates for those spectra without measurable [O III] emission and those for which the [O III] line was redshifted beyond 9200 Å. We used a χ^2 minimization technique, similar to that used by Franx, Illingworth & Heckman (1989) to measure the redshifts. A low-order polynomial was fit to the composite and to each spectrum to approximate a continuum, then subtracted. The composite spectrum was shifted in small redshift steps and compared to the individual quasar spectra. The redshift which minimized χ^2 – the sum of the squared inverse-variance weighted residuals – was taken as the systemic redshift. Quasars with χ^2 and manual redshifts which differed by more than twice the dispersion of the velocity differences of the entire sample (about $700\,\mathrm{km\,s^{-1}}$) were examined for possible causes unrelated to the properties of the quasar. Spectra with identified problems were either corrected (if possible) or rejected. A new composite was then made using all of the spectra with either χ^2 or [O III] redshifts. The template matching and recombining process was done in several progressively higher redshift ranges, so that there was sufficient overlap between

the templates and the input spectra that included at least two strong emission lines.

3.2. Generating the Composite Spectra

Both median and geometric mean composite spectra were then generated for the analysis of emission features and the global continuum respectively. The final set of spectra were shifted to the rest frame using the refined redshifts, then rebinned onto a common wavelength scale at 1 Å per bin, which is roughly the resolution of the observed spectra shifted to the rest frame. The number of quasar spectra which contribute to each 1 Å bin is shown as a function of wavelength in Fig. 2. The median spectrum was constructed from the entire data set in the same way as the [O III] composite, as described in the previous section. The spectral region blueward of the Ly α emission line was ignored when calculating the flux density scaling, since the Ly α forest flux density varies greatly from spectrum to spectrum. The final spectrum was truncated to 800Å on the short wavelength end, since there was little or no usable flux in the contributing spectra at shorter wavelengths. The median flux density values of the shifted, rebinned, and scaled spectra were determined for each wavelength bin to form the final median composite quasar spectrum, shown in Fig. 3 on a logarithmic scale. An error array was calculated by dividing the 68% semi-interquantile range of the flux densities by the square root of the number of spectra contributing to each bin. This estimate agrees well with the uncertainty determined by measuring the variance in relatively featureless sections of the combined spectrum. The median spectrum extends from 800 – 8555 Å in the rest frame. Figure 4 shows the S/N per 1 Å bin, which approaches 330 at 2800 Å. The wavelength, flux density, and uncertainty arrays of the median spectrum are given in Table 1, which is available as an electronic journal table.

To generate the geometric mean spectrum, the shifted and rebinned spectra were normalized to unit average flux density over the rest wavelength interval 3020 – 3100 Å, which contains no strong narrow emission lines, and which is covered by about 90% of the spectra. The restriction that the input spectra cover this interval results in a combined spectrum which ranges from about 1300 – 7300Å, and is composed of spectra with redshifts from $z = 0.26 - 1.92$. The geometric mean of the flux density values was calculated in each wavelength bin to form the geometric mean composite quasar spectrum, shown in Fig. 5 on a logarithmic scale. The median and geometric mean composites are quite similar, but there are subtle differences in both the continuum slopes and the emission line profiles, discussed further in the next sections, which justify the construction of both composite spectra.

4. Continuum, Emission, and Absorption Features

4.1. The Continuum

The geometric mean spectrum is shown on a log-log scale in Fig. 5, where a single power-law will appear as a straight line. The problem of fitting the quasar continuum is complicated by the fact that there are essentially no emission-line-free regions in the spectrum. Our approach is to find a set of regions which give the longest wavelength range over which a power law fit does not cross the spectrum (i.e. the end points of the fit are defined by the two most widely separated consecutive intersections). The regions which satisfy this are $1350 - 1365$ Å and $4200 - 4230$ Å. A single power-law fit through the points in those regions gives an index of $\alpha_\nu = -0.44$ ($\alpha_\lambda = -1.56$), and fits the spectrum reasonably well from just redward of Ly α to just blueward of H β (Fig. 5). The statistical uncertainty in the spectral index from the fit alone is quite small (≈ 0.005) owing to the high S/N of the spectrum and the wide separation of the fitted regions. However, the value of the index is sensitive to the precise wavelength regions used for fitting. More importantly, the spectrophotometric calibration of the spectra introduces an uncertainty of ≈ 0.1 in α_ν (§ 2). We estimate the uncertainty of the measured value of the average continuum index to be ≈ 0.1, based mainly on the remaining spectral response uncertainties. Redward of H β the continuum flux density rises above the amount predicted by the power-law; this region is better fit by a separate power-law with an index of $\alpha_\nu = -2.45$ ($\alpha_\lambda = 0.45$) (Fig. 5), which was determined using the wavelength ranges $6005 - 6035$Å and $7160 - 7180$Å. The abrupt change in the continuum slope is discussed in § 5.

As a comparison, we have also measured the power-law indices for the *median* composite, which are $\alpha_\nu = -0.46$ ($\alpha_\lambda = -1.54$) and $\alpha_\nu = -1.58$ ($\alpha_\lambda = -0.42$) for the respective wavelength regions (Fig. 3). The index found for the Ly α to H β region is almost indistinguishable from that found for the geometric mean composite. The indices for both spectra redward of H β are significantly different however, and are a result of the different combining processes. The geometric mean should give a better estimate of the average index, but comparison with mean or median composite spectra from other studies is probably reasonable in the Ly α to H β region, given the small difference in the indices measured for our composite spectra. The continuum blueward of the Ly α emission line is heavily absorbed by Ly α forest absorption, as seen in Fig. 3. However, because the strength of the Ly α forest is a strong function of redshift, and a large range of redshifts was used in constructing the sample, no conclusions can be drawn about the absorption or the continuum in that region.

4.2. Emission and Absorption Lines

The high S/N and relatively high resolution (1 Å) of the composite allows us to locate and identify weak emission features and resolve some lines that are often blended in other composites. It is also possible that our sample includes a higher fraction of spectra with narrower line profiles,

which could also help in distinguishing emission features. For example, close lines that are clearly distinguished in the spectrum include Hα/[N II] ($\lambda\lambda$6548, 6563, 6583), Si III]/C III] ($\lambda\lambda$1892, 1908), the [S II] ($\lambda\lambda$6716, 6730) doublet, and Hγ/[O III] ($\lambda\lambda$4340, 4363). Emission line features above the continuum were identified manually in the median spectrum. Including the broad Fe II and Fe III complexes, 85 emission features were detected. The end points of line positions, λ_{lo} and λ_{hi}, were estimated to be where the flux density was indistinguishable from the local "continuum". The local continuum is not necessarily the same as the power-law continuum estimated in § 4.1, since the emission lines may appear to lie on top of other emission lines or broad Fe II emission features. The peak position of each emission line, λ_{obs}, was estimated by calculating the mode of the top $\approx 50\%$ of the line – the same method used for measuring the [O III] λ5007 line peaks in § 3.1. Uncertainties in the peak positions include the contribution from the flux-densisty uncertainties, but none from uncertainties in the local continuum estimate. Fluxes and equivalent widths were measured by integrating the line flux density between the end points and above the estimated local continuum. Line profile widths were estimated by measuring the rms wavelength dispersion, σ_λ, about the peak position – i.e. the square-root of the average flux-weighted squared differences between the wavelength of each pixel in a line profile and the peak line position. Asymmetry of the line profiles was measured using Pearson's skewness coefficient, skewness $= 3 \times (\mathrm{mean} - \mathrm{median})/\sigma_\lambda$. Lines were identified by matching wavelength positions and relative strengths of emission features found in other objects, namely the Francis et al. (1991) composite, the Zheng et al. (1997) composite, the narrow-lined quasar I Zw 1 (Laor, Jannuzi, Green & Boroson 1997; Oke & Lauer 1979; Phillips 1976), the ultra-strong Fe II emitting quasar 2226-3905 (Graham, Clowes & Campusano 1996), the bright Seyfert 1 galaxy NGC 7469 (Kriss, Peterson, Crenshaw & Zheng 2000), the high-ionization Seyfert 1 galaxy III Zw 77 (Osterbrock 1981), the extensively observed Seyfert 2 galaxy NGC 1068 (Snijders, Netzer & Boksenberg 1986), the powerful radio galaxy Cygnus A (Tadhunter, Metz & Robinson 1994), and the Orion Nebula HII region (Osterbrock, Tran & Veilleux 1992). Identification of many Fe II complexes was made by comparison with predicted multiplet strengths by Verner et al. (1999); Netzer & Wills (1983); Grandi (1981); and Phillips (1978), and multiplet designations are taken from those references. Table 2 lists the detected lines, their vacuum wavelength peak positions, relative fluxes, equivalent widths, profile widths, skewness, and identifications. Rest wavelengths were taken from the Atomic Line List[28]. Wavelengths of lines consisting of multiple transitions were found by taking the oscillator-strength weighted average in the case of permitted lines, and the adopted values from the above references for forbidden lines. In all cases, the permitted rest wavelength values agreed with the (vacuum) values adopted in the above references. Fig. 6 shows an expanded view of the quasar composite on a log-linear scale with the emission features labeled.

It is clear from Fig. 6 that most of the UV-optical continuum is populated by emission lines. Most strong emission lines show "contamination" by blends with weaker lines, as seen in the expanded profiles of 12 emission line regions in Fig. 7. The very broad conspicuous feature from

[28]The Atomic Line List is hosted by the Department of Physics and Astronomy at the University of Kentucky; (`http://www.pa.uky.edu/~peter/atomic/`).

$\approx 2200 - 4000$ Å is known as the 3000 Å bump (Grandi 1982; Oke, Shields & Korycansky 1984), and consists of blends of Fe II line emission and Balmer continuum emission (Wills, Netzer & Wills 1985). The Fe II and Fe III complexes are particularly ubiquitous, and contribute a large fraction of the emission line flux. Using this composite, these complexes have been shown to be an important contributor to the color-redshift relationships of quasars (Richards et al. 2001a).

Several absorption features often seen in galaxies are also identifiable in the median composite quasar spectrum. These lines are listed in Table 3 along with several measured quantities, and include H 9 λ3835, H 10 λ3797, the Ca II λ3933 K line, and Ca II $\lambda\lambda$8498, 8542 – two lines of a triplet (the second-weakest third component would fall beyond the red end of the spectrum). The MgI $\lambda\lambda$5167, 5172, 5183 triplet lines may also be present in the spectrum, but they would lie inside a strong complex of FeII emission and near several other expected emission lines. The locations of other common stellar absorption lines seen in galaxies, such as the lower-order Balmer lines and the Ca II λ3968 H line, are dominated by emission lines. The presence of stellar absorption lines argues for at least some host galaxy contamination in the quasar composite spectrum, despite the fact that we rejected objects with obvious stellar lines in individual galaxies. To examine this further, we have created a low-redshift median composite using only quasars with redshifts $z_{em} \leq 0.5$, which is almost equivalent to selecting only quasars with restframe absolute r' magnitude $M_{r'} \geq -21.5$ (calculated using a spectral index of $\alpha_\nu = -0.44$). The low-z composite covers a rest wavelength range of $2550 - 8555$Å. The absorption lines found in the low-z spectrum are marked in Fig. 8, and listed in Table 3. More absorption lines are detected in the low-z composite spectrum than the full-dataset spectrum, and the lines in common are stronger in the low-z spectrum – as expected if host galaxy contamination is the source of the absorption lines. We discuss the absorption lines in more detail in § 5.

The 2175Å extinction bump often seen in the spectra of objects observed through the Galactic diffuse interstellar medium, and usually attributed to graphite grains (Mathis, Rumpl & Nordsieck 1977), is not present at a detectable level in the composite spectrum. This agrees with the non-detection of the feature by Pitman, Clayton & Gordon (2000) who searched for it in other quasar spectral composites.

4.3. Systematic Line Shifts

Because the composite was constructed using redshifts based upon a single emission line position ([O III] λ5007) or cross-correlations with an [O III]-based composite, we can check for systematic offsets between the measured peak positions and the [O III]-based wavelengths. Several emission lines – C IV λ1549 for example – are offset from their laboratory wavelengths, as evident from Fig. 7. Such line shifts have been detected previously (e.g. Grandi 1982; Wilkes 1986; Tytler & Fan 1992; Laor et al. 1995; McIntosh, Rix, Rieke & Foltz 1999), and are present for many of the lines listed in Table 2. Real line position offsets can be confused with apparent "shifts" which can arise from several sources, including contamination by line blends, incorrect identifications, and line asymme-

try. To minimize these problems, we have selected only relatively strong lines with isolated peaks, and we have re-measured the peaks of only the top 25% of the line flux for lines which appeared to have a very broad component or asymmetric profile. The velocity shifts for the selected lines are listed in Table 4. A negative velocity indicates that a line is blueshifted with respect to the nominal laboratory wavelength, and visa-versa. By design, the [O III] λ5007 line peak shows no shift from its laboratory rest wavelength to well within the measurement uncertainty. All other emission line peaks are measured with respect to the rest frame of the [O III] λ5007 line. The two other measurable [O III] lines, λ4363 and λ4958, have no velocity shift to within the uncertainties.

It has been suggested that there is a correlation between the line shift and the ionization energy of the species (e.g. Tytler & Fan 1992; McIntosh, Rix, Rieke & Foltz 1999). Quasar emission lines are generally separated into two broad categories: the permitted and semi-forbidden lines which are typically broad ($FWHM > 500\,\mathrm{km\,s^{-1}}$), and the much narrower forbidden lines. These classes of lines are thought to arise from physically distinct regions: the parsec-scale Broad Line Region (BLR) and the kiloparsec-scale Narrow Line Region (NLR) respectively. Since their origins are likely to be different, we treat the BLR and NLR lines separately. Figure 9 shows the ionization energy vs. velocity shifts in Table 4 both for the BLR lines, and the NLR lines, labeled by their ions. In both cases, there is an apparent anti-correlation between the velocity shifts and ionization potential in Fig. 9. The Spearman rank correlation coefficient for the BLR lines gives a random probability of finding as strong a correlation at about 0.6%. We have taken the uncertainties in the velocity measurements into account, by creating 10^4 mock data sets of velocities, randomly distributed for each emission line according to the velocity uncertainties, then recalculated the correlation probabilities. For half of the mock datasets, the random probability of a correlation was less than 1.6% for the BLR lines. Thus we would have found a significant anti-correlation between the velocity offsets and ionization potentials for a majority of independent measurements. The low-ionization C II λ1335 line has the maximum redshift at $292\,\mathrm{km\,s^{-1}}$, and the high-ionization C IV λ1549 line has the maximum blueshift at $-564\,\mathrm{km\,s^{-1}}$. The N V point appears to be somewhat of an outlier, possibly due to severe blending with Ly α . It is also interesting that N V does not follow the Baldwin effect (Espey & Andreadis 1999), the strength of which is otherwise anti-correlated with ionization potential. In any case, the rank correlation of the velocity offset and ionization potential is not significantly stronger when N V it is removed, and we have no compelling reason to do so. The velocity offsets are not as strong for the NLR lines – $\lesssim 100\,\mathrm{km\,s^{-1}}$ – but the Spearman rank correlation probability is 1.3×10^{-4}, which is quite significant, and we find the probability is less than 1% for half of the mock data sets. We discuss emission line velocity shifts further in § 5.

4.4. Spectrum-to-spectrum Differences

While constructing the median composite, the flux levels of overlapping spectra were scaled so that the integrated flux densities were the same. Thus we expect the variation in the continuum flux density across the spectrum to reflect the spectrum-to-spectrum differences caused by differing

continuum shapes and emission line fluxes and profiles. (This does not, however, address spectral *time* variability.) Fig. 10 shows the 68% semi-interquantile range divided by the median spectrum, after the contribution from the combined flux density uncertainties of each spectrum were removed in quadrature. The individual spectral uncertainties include statistical noise estimates, but not uncertainties in the (un-finalized) flux calibration. The largest relative variations from the median spectrum occur in the narrow emission lines such as the [O III] $\lambda\lambda 4958, 5007$ lines, and the cores of broad emission lines such as C IV $\lambda 1549$ and Ly α $\lambda 1215$. Variations of the broad components of H α $\lambda 6563$ and Mg II $\lambda 2798$ are evident, but less so for H β $\lambda 4861$ and C IV $\lambda 1549$, and there is little sign of variation in the C III] $\lambda 1908$ line. Most of the broad Fe II complexes show significant variation. The Ly α forest region varies considerably, as expected, since structure in the forest can be partly resolved in the individual spectra, and the forest strength changes with redshift so the combination of spectra at different redshifts will naturally give rise to a high variance. An additional feature of some interest is the pair of variation peaks at 3935 Å and 3970 Å, which correspond precisely to the Ca II doublet. These are detected in absorption in the median composites (although [Ne III] and H ϵ emission interfere with Ca II$\lambda 3970$), and the variation may indicate that spectral contamination by the host galaxy is fairly common. A full analysis of spectrum-to-spectrum variations requires other means such as principal component analysis (Boroson & Green 1992; Francis, Hewett, Foltz & Chaffee 1992; Brotherton, Wills, Francis & Steidel 1994; Wills et al. 1999), which we plan for a future project.

5. Discussion

The Large Bright quasar Survey (LBQS) composite (kindly provided by S. Morris) updated from Francis et al. (1991), the First Bright quasar Survey (FBQS) composite (available electronically, Brotherton et al. (2000)), and our median composite, are shown for comparison in Fig. 11. The spectra have been scaled to unit average flux density in the range $3020 - 3100$Å. All three spectra are quite similar in appearance except for slight differences. The strength of the Ly α line and some of the narrow emission lines in the FBQS composite are stronger than for the other composites. The difference is probably due to that fact that the FBQS sample is entirely radio selected, and there is a correlation between line strengths and radio loudness (Boroson & Green 1992; Francis, Hewett, Foltz & Chaffee 1992; Brotherton, Wills, Francis & Steidel 1994; Wills et al. 1999). Otherwise, the relative fluxes are similar for the lines in common among the various composites. The higher resolution and higher S/N of our composite has allowed us to identify many more lines than listed for the other spectra (although a number of the features we find are present at a lower significance level in the other spectra). We have identified a total of 85 emission features in the median spectrum. All of the features have been identified in other quasar or AGN spectra, but not in any single object. A large number of the identified features are attributed to either Fe II or Fe III multiplets. The combination of these features has been shown to greatly affect the color-redshift relationship for quasars (Richards et al. 2001a).

A single power-law is an adequate fit to the continuum between Ly α and H β , especially given the predicted strengths of the Fe II and Fe III emission line complexes in that range (Verner et al. 1999; Netzer & Wills 1983; Laor, Jannuzi, Green & Boroson 1997). The index we find, $\alpha_\nu = -0.44$, is in good agreement with most recent values found in optically-selected quasar samples. Table 5 lists average power-law indices from various sources over the past decade. The LBQS composite, FBQS composite, and Hubble Space Telescope (HST) composite (Zheng et al. 1997) spectra are available electronically, so for consistency, we have also remeasured the power-law indices of those spectra using the technique described in § 4.1. The remeasured values are not significantly different from the values given in the papers.

Most of the composite measurements agree with averages over continuum fits to individual spectra. One outlier is the measurement by Zheng et al. (1997), who find a steeper (redder) continuum with $\alpha_\nu = -0.99$ using a composite made with spectra from HST. The difference is attributed to the lower redshift of the Zheng et al. (1997) quasar sample and a correlation between redshift and steeper UV continuum (Francis 1993). To test this, we have created a low-redshift geometric mean composite using only those quasars which cover a rest wavelength of 5000 Å ($z < 0.84$). Since the 1350Å wavelength region we have used to measure continuum slopes is not covered by the low-z composite, we used instead the flux density in the wavelength range $3020 - 3100$Å multiplied by a factor of 0.86, which is the ratio of the flux density of the power-law fit to the flux density of the spectrum for the full-sample geometric mean composite in that range. We find a steeper index for the low-redshift composite, $\alpha_\nu = -0.65$, than for the full-sample composite, $\alpha_\nu = -0.44$, although the difference is not as great as with the Zheng et al. (1997) composite.

Another apparently discrepant value is the result from Schneider et al. (2001), who find $\alpha_\nu = -0.93$ for a sample of very high-redshift quasars. Similar values for high-z samples have been found by Fan et al. (2001) and Schneider, Schmidt & Gunn (1991). The steep indices measured for high-z quasars may be due to the restricted wavelength range typically used in fitting the continua, as suggested by Schneider et al. (2001), and not to a change in the underlying spectral index at high redshift. At high redshifts, only relatively short wavelength ranges redward of Ly α are avaliable in optical spectra, and these tend to be populated by broad Fe II and Fe III complexes. If, for example, the regions of the median composite near 1350Å and 1600Å (just redward of the C IV emission line) are taken as continuum (as Schneider et al. (2001) did), we find a power-law index of $\alpha_\nu = -0.93$. This example demonstrates the generic difficulty of measuring continuum indices without a very large range of wavelength, or some estimate of the strength of the contribution from blended emission lines.

The continuum slope changes abruptly near 5000 Å and becomes steeper with an index of $\alpha_\nu = -2.45$, which is a good fit up to the red end of the spectrum (8555 Å). This change is also evident in the FBQS composite, and has been noted in the spectra of individual quasars (Wills, Netzer & Wills 1985). An upturn in the spectral energy distribution of quasars – the so-called near-infrared inflection, presumably caused by emission from hot dust – has been seen starting between 0.7 and 1.5μm (e.g. Neugebauer et al. 1987; Elvis et al. 1994). This may be in part what

we are seeing at wavelengths beyond ≈ 5000Å, but it is unlikely that the sublimation temperature of dust would be high enough for the emission to extend to wavelengths below 6000Å (Puget, Leger, & Boulanger 1985; Efstathiou, Hough, & Young 1995).

Another possible contributor to the long wavelength steepening is contamination from the host galaxies. The 3″ optical fiber diameter subtends much if not all of the host galaxy image, even for the lowest redshift quasars. The best evidence for the contribution of host galaxy light is the presence of stellar absorption lines in the composite spectra. The lines become stronger as the redshift, and equivalently, luminosity, distributions of the quasar sample are lowered. This is seen by comparing the absorption line strengths of the low-redshift median composite (§ 4.2) with the full-sample composite. The strengths of the absorption lines in the low-redshift median composite, assuming a typical elliptical galaxy spectrum, imply a contribution to the composite quasar light from stars of about $7-15\%$ at the locations of Ca II $\lambda 3933$ and Na I $\lambda 5896$, and about 30% at the locations of Ca II $\lambda\lambda 8498, 8542$. The trend of a greater contribution from starlight with increasing wavelength is expected because the least luminous quasars, in which the relative host galaxy light is presumably most important, contribute the majority of spectra to the composite at longer wavelengths. This trend has also been seen in the spectral light from the nuclei of individual low-redshift Seyfert galaxies and other AGN (Terlevich, Diaz, & Terlevich 1990; Serote Roos, Boisson, Joly, & Ward 1998), which suggest a significant contribution from starburst activity dominated by red supergiants (Cid Fernandes & Terlevich 1995). The mean absolute r' magnitude of the quasars making up the low-z composite is $M_{r'} = -21.7$ (Fig. 1), which implies a host galaxy magnitude of about $M_{r'} = -19.2$ (assuming a host contribution of $\sim 10\%$) – a moderately luminous value in the SDSS filter system (Blanton et al. 2001). We conclude that both stellar light from the host galaxies and a real change in the quasar continuum cause the steepening of the spectral index beyond 5000Å.

The detection of stellar Balmer absorption lines implies that young or intermediate age stars make a substantial contribution to the light of the host galaxies. This is at odds with the conclusions based on host-galaxy spectra (Nolan et al. 2001), and two-dimensional image modeling (McLure et al. 1999; McLure & Dunlop 2000) that the hosts of quasars and radio galaxies are "normal" giant ellipticals. The discrepancy cannot immediately be attributed to redshift differences, since the McLure & Dunlop (2000) sample extends to $z \approx 1$, and we detect Balmer absorption lines in the full-sample composite with a mean redshift of $z = 1.25$. More likely, the difference is due to the fact that our spectra include only the inner 3″ of the galaxy light while the spectra taken by Nolan et al. (2001) sample only off-nuclear (5″ from nucleus) light, and the image modeling includes the entire profile of the galaxies. This suggests that the stellar population near the nuclei of quasar host galaxies – near the quasars themselves – is substantially younger than that of the host galaxies.

Velocity shifts in the BLR lines relative to the forbidden NLR lines – taken to be at the systemic host-galaxy redshift – are seen for most quasars and are similar to the values we find for the composite BLR lines relative to [O III] $\lambda 5007$ (e.g. Tytler & Fan 1992; Laor et al. 1995; McIntosh, Rix, Rieke & Foltz 1999). The origin of the shifts is not known, but explanations

include gas inflows and outflows (e.g. Gaskell 1982; Corbin 1990), attenuation by dust (Grandi 1977; Heckman, Butcher, Miley & van Breugel 1981), relativistic effects (Netzer 1977; Corbin 1995, 1997; McIntosh, Rix, Rieke & Foltz 1999), and line emission from physically different locations (e.g. Espey et al. 1989). The magnitudes of the shifts seem to depend upon the ionization energies (Gaskell 1982; Wilkes 1986; Espey et al. 1989; Tytler & Fan 1992; McIntosh, Rix, Rieke & Foltz 1999) in the sense that more negative velocities (blueshifts) are seen for higher ionization lines. We have confirmed this correlation using a large number of BLR lines (§ 4.3).

It is often assumed that the NLR lines are at the systemic redshift of the quasar, since the lines are thought to originate in a kpc-scale region centered on the quasar, and the lines show good agreement (to within $100\,\mathrm{km\,s^{-1}}$) with the redshifts of host galaxies determined by stellar absorption lines (Gaskell 1982; Vrtilek & Carleton 1985), and H I 21 cm observations (Hutchings, Gower & Price 1987). However, for some of the higher-ionization forbidden lines, such as [O III] λ5007, Ne V λ3426, Fe VII λ6086, Fe X λ6374, and Fe XI λ7892, seen in quasars and Seyfert galaxies, significant velocity shifts, usually blueshifts, have been detected in the past (Heckman, Butcher, Miley & van Breugel 1981; Mirabel & Wilson 1984; Penston et al. 1984; Whittle 1985; Appenzeller & Wagner 1991, e.g.). The large number (17) of NLR lines we have been able to measure cover a wide range in ionization potentials. These lines are shifted with respect to one another and the shifts are correlated with ionization energy. This appears to be a real effect, since we have been careful to select only those lines which have well-defined non-blended peaks. Another verification of the accuracy of the velocity measurements is that lines originating from the same ion but at different rest wavelengths almost always have consistent velocity offsets within the measurement uncertainties (Table 4 & Fig. 9).

The NLR velocity shifts and their correlation with ionization potential suggest that the same mechanism responsible for the shifts of the BLR lines also applies to the NLR lines, although the effect is weaker. One possible explanation is that the BLR contains some lower density forbidden line emitting gas, as first suggested by Penston (1977). The correlation is strong, but the effect is subtle, so follow-up work will likely have to involve both higher quality optical spectra and observations in the near-IR in order to detect a sufficient sample of narrow forbidden lines.

We have implicitly assumed that the velocity differences are independent of other factors such as redshift and luminosity. However, McIntosh, Rix, Rieke & Foltz (1999) found that higher-z quasars tend to have greater velocity offsets relative to the [O III] line. For quasars in our sample with $z > 0.84$, the [O III] emission line is redshifted out of the spectra, which is why we used a cross-correlation technique to estimate the center-of-mass redshifts. If the true velocity offsets depend upon redshift, the relation will be weakened by the cross-correlation matching which finds the best match to a lower-redshift template, and thus will tend to yield the lower-redshift emission line positions. A desirable future project is extending the wavelength coverage to the near-infrared at higher redshift and to the ultraviolet at lower redshift in order to simultaneously detect low and high velocity lines. Such a program of even a relatively modest sample size would be highly beneficial to many quasar studies.

6. Summary

We have created median and geometric mean composite quasar spectra using a sample of over 2200 quasars in the Sloan Digital Sky Survey. The resolution and signal to noise ratio exceed all previously published UV/optical quasar composites. Over 80 emission line features have been detected and identified. We have been able to measure velocity shifts in a large number of both permitted and forbidden emission line peaks, most of which have no such previous measurements. Power-law fits to the continua verify the results from most recent studies. The composites show that there is a lack of emission-free regions across most of the UV/optical wavelength range, which makes fitting quasar continua difficult unless a very wide wavelength range is available.

The SDSS is rapidly producing high-quality spectra of quasars which cover a wide range of properties. Composite spectra can therefore be made from numerous sub-samples in order to search for dependencies of global spectral characteristics on a variety of quasar parameters, such as redshift, luminosity, and radio loudness – a program which is currently underway. We are also using other techniques such as principal component analysis to examine trends among the diversity of quasar spectra.

The median composite is being used as a cross-correlation template for spectra in the SDSS, and many other applications are imaginable. The median composite spectrum is likely to be of general interest, so it is available as an electronic table (Table 1).

The Sloan Digital Sky Survey (SDSS)[29] is a joint project of The University of Chicago, Fermilab, the Institute for Advanced Study, the Japan Participation Group, The Johns Hopkins University, the Max-Planck-Institute for Astronomy, New Mexico State University, Princeton University, the United States Naval Observatory, and the University of Washington. Apache Point Observatory, site of the SDSS telescopes, is operated by the Astrophysical Research Consortium (ARC). Funding for the project has been provided by the Alfred P. Sloan Foundation, the SDSS member institutions, the National Aeronautics and Space Administration, the National Science Foundation, the U.S. Department of Energy, Monbusho, and the Max Planck Society. We thank Simon Morris for making an electronic version of the LBQS composite quasar spectrum available to us, and Bev Wills for helpful comments. MAS acknowledges support of NSF grant AST-0071091. DPS and GTR acknowledges support of NSF grant AST-990703.

[29]The SDSS Web site is `http://www.sdss.org/`.

Table 1. Median Composite Quasar Spectrum[a]

λ (Å)	f_λ (Arbitrary Units)	f_λ Uncertainty (Arbitrary Units)
800.5	0.149	0.074
801.5	0.000	0.260
802.5	0.676	0.227
803.5	0.000	0.222
804.5	0.413	0.159
805.5	0.338	0.326
806.5	0.224	0.159
807.5	0.122	0.360
808.5	0.612	0.346
809.5	0.752	0.304
810.5	0.197	0.257
811.5	0.187	0.189
812.5	0.000	0.126
813.5	0.000	0.171
814.5	0.502	0.181

Note. — The complete version of this table will appear in the electronic edition of the Journal. The printed edition contains only a sample. The full table can be found temporarily at `ftp://sdss.fnal.gov/pub/danvb/qsocomposite/sdss_qso_median.tab1`

Table 2. Composite Quasar Emission Line Features

λ_{obs} (Å)	λ_{lo} (Å)	λ_{hi} (Å)	Rel. Flux $100\times F/F(\mathrm{Ly}\alpha)$	W (Å)	Width σ_λ(Å)	Skew	ID[a]	λ_{lab} (Å) or Multiplet[b]
940.93 ± 3.17	930	955	2.110 ± 0.379	2.95 ± 0.54	4.73	0.59	Lyϵ:	937.80
							Lyδ:	949.74
985.46 ± 4.78	960	1003	5.195 ± 0.459	6.55 ± 0.58	8.95	−0.51	CIII	977.02
							NIII	990.69
1033.03 ± 1.27	1012	1055	9.615 ± 0.484	9.77 ± 0.49	7.76	−0.01	Lyβ	1025.72
							OVI	1033.83
1065.10 ± 5.09	1055	1077	0.816 ± 0.269	0.80 ± 0.27	4.17	0.30	ArI	1066.66
1117.26 ± 2.78	1100	1140	3.151 ± 0.289	3.66 ± 0.34	8.49	0.02	FeIII:	UV1
1175.35 ± 1.17	1170	1182	0.870 ± 0.148	0.83 ± 0.14	2.28	−0.01	CIII*	1175.70
1216.25 ± 0.37	1160	1290	100.000 ± 0.753	92.91 ± 0.72	19.46	0.40	Lyα	1215.67
1239.85 ± 0.67	1230	1252	2.461 ± 0.189	1.11 ± 0.09	2.71	−0.21	NV	1240.14
1265.22 ± 3.20	1257	1274	0.306 ± 0.081	0.21 ± 0.06	2.74	0.25	SiII	1262.59
1305.42 ± 0.71	1290	1318	1.992 ± 0.076	1.66 ± 0.06	5.42	−0.21	OI	1304.35
							SiII	1306.82
1336.60 ± 1.13	1325	1348	0.688 ± 0.059	0.59 ± 0.05	3.86	−0.02	CII	1335.30
1398.33 ± 0.31	1360	1446	8.916 ± 0.097	8.13 ± 0.09	12.50	0.06	SiIV	1396.76
							OIV]	1402.06
1546.15 ± 0.14	1494	1620	25.291 ± 0.106	23.78 ± 0.10	14.33	−0.04	CIV	1549.06
1637.84 ± 0.83	1622	1648	0.521 ± 0.027	0.51 ± 0.03	4.43	−0.22	HeII	1640.42
1664.74 ± 1.04	1648	1682	0.480 ± 0.028	0.50 ± 0.03	5.50	0.11	OIII]	1663.48
							AlII	1670.79
							FeII	UV40
1716.88 ± 2.83	1696	1736	0.258 ± 0.027	0.30 ± 0.03	7.36	0.17	NIV	1718.55
							FeII	UV37
							AlII	1721.89
1748.31 ± 0.75	1735	1765	0.382 ± 0.021	0.44 ± 0.03	5.12	0.04	NIII]	1750.26
1788.73 ± 0.98	1771	1802	0.229 ± 0.020	0.28 ± 0.02	6.06	−0.29	FeII	UV191
1818.17 ± 2.07	1802	1831	0.130 ± 0.019	0.16 ± 0.02	5.72	−0.47	SiII	1816.98
							[NeIII]	1814.73
1856.76 ± 1.18	1840	1875	0.333 ± 0.021	0.40 ± 0.03	4.95	0.01	AlIII	1857.40
1892.64 ± 0.83	1884	1900	0.158 ± 0.015	0.16 ± 0.02	3.09	−0.10	SiIII]	1892.03
							FeIII	UV34
1905.97 ± 0.12	1830	1976	15.943 ± 0.041	21.19 ± 0.05	23.58	−0.27	CIII]	1908.73
							FeIII	U34
							FeIII	UV68
							FeIII	UV61
1991.83 ± 2.91	1976	2008	0.139 ± 0.014	0.20 ± 0.02	6.73	−0.03	FeIII	UV50
2076.62 ± 0.78	2036	2124	1.580 ± 0.021	2.46 ± 0.03	16.99	0.18	FeIII	UV48
2175.62 ± 1.83	2153	2199	0.143 ± 0.013	0.25 ± 0.02	5.85	0.46	FeII	UV79
							FeII	UV370
2222.29 ± 1.44	2202	2238	0.185 ± 0.011	0.33 ± 0.02	6.98	−0.11	FeII	UV118
							FeII	UV376
2324.58 ± 0.56	2257	2378	2.008 ± 0.020	3.56 ± 0.04	22.23	−0.29	FeII	many
2327.34 ± 0.72	2312	2338	0.183 ± 0.009	0.31 ± 0.02	4.95	−0.41	CII]	2326.44
2423.46 ± 0.44	2402	2448	0.437 ± 0.012	0.77 ± 0.02	8.42	0.25	[NeIV]	2423.83
							FeIII	UV47
2467.98 ± 1.59	2458	2482	0.092 ± 0.009	0.16 ± 0.02	4.54	0.30	[OII]	2471.03
							FeII	UV395

Table 2—Continued

λ_{obs} (Å)	λ_{lo} (Å)	λ_{hi} (Å)	Rel. Flux $100\times F/F(\mathrm{Ly}\alpha)$	W (Å)	Width σ_λ(Å)	Skew	ID[a]	λ_{lab} (Å) or Multiplet[b]
2626.92 ± 0.99	2595	2654	0.398 ± 0.013	0.81 ± 0.03	9.93	0.00	FeII	UV1
2671.89 ± 1.78	2657	2684	0.067 ± 0.008	0.14 ± 0.02	5.10	0.05	AlII]	2669.95
							OIII	2672.04
2800.26 ± 0.10	2686	2913	14.725 ± 0.030	32.28 ± 0.07	34.95	−0.06	MgII	2798.75
2964.28 ± 0.79	2910	3021	2.017 ± 0.017	4.93 ± 0.04	22.92	−0.03	FeII	UV78
3127.70 ± 1.07	3100	3153	0.326 ± 0.012	0.86 ± 0.03	9.38	−0.13	OIII	3133.70
							FeII	Opt82
3191.78 ± 0.99	3159	3224	0.445 ± 0.013	1.17 ± 0.03	12.77	−0.04	HeI	3188.67
							FeII	Opt6
							FeII	Opt7
3261.40 ± 2.70	3248	3272	0.032 ± 0.008	0.09 ± 0.02	3.27	0.06	FeI	Opt91
							FeII	Opt1
3281.74 ± 3.15	3272	3297	0.036 ± 0.008	0.10 ± 0.02	4.39	0.56	FeII	Opt1
3345.39 ± 0.75	3329	3356	0.118 ± 0.008	0.35 ± 0.02	5.50	−0.41	[NeV]	3346.82
3425.66 ± 0.46	3394	3446	0.405 ± 0.012	1.22 ± 0.04	9.09	−0.62	[NeV]	3426.84
3498.92 ± 1.60	3451	3537	0.432 ± 0.014	1.38 ± 0.05	16.79	−0.24	FeII	Opt4
							FeII	Opt16
3581.70 ± 4.48	3554	3613	0.100 ± 0.011	0.34 ± 0.04	7.98	0.79	[FeVII]	3587.34
							HeI	3588.30
3729.66 ± 0.18	3714	3740	0.424 ± 0.009	1.56 ± 0.03	3.32	−0.24	[OII]	3728.48
3758.46 ± 0.56	3748	3771	0.078 ± 0.007	0.29 ± 0.03	3.71	0.12	[FeVII]	3759.99
3785.47 ± 1.31	3775	3799	0.056 ± 0.006	0.22 ± 0.03	4.24	0.13	FeII:	Opt15
3817.41 ± 2.46	3800	3832	0.124 ± 0.007	0.51 ± 0.03	7.33	−0.10	FeII:	Opt14
3869.77 ± 0.25	3850	3884	0.345 ± 0.008	1.38 ± 0.03	5.31	−0.50	[NeIII]	3869.85
3891.03 ± 1.28	3882	3898	0.020 ± 0.005	0.08 ± 0.02	2.02	−0.27	HeI	3889.74
							H 8	3890.15
3968.43 ± 0.91	3950	3978	0.104 ± 0.007	0.45 ± 0.03	5.32	−0.62	[NeIII]	3968.58
							H ϵ	3971.20
4070.71 ± 1.18	4061	4079	0.039 ± 0.005	0.18 ± 0.03	3.20	0.01	[FeV]	4072.39
							[SII]	4073.63
4102.73 ± 0.66	4050	4152	1.066 ± 0.013	5.05 ± 0.06	18.62	0.03	H δ	4102.89
4140.50 ± 0.96	4135	4145	0.026 ± 0.004	0.13 ± 0.02	1.83	−0.38	FeII	Opt27
							FeII	Opt28
4187.55 ± 1.97	4157	4202	0.154 ± 0.009	0.76 ± 0.04	9.77	−0.40	FeII	Opt27
							FeII	Opt28
4239.85 ± 2.07	4227	4260	0.107 ± 0.008	0.53 ± 0.04	5.73	−0.05	[FeII]	Opt21F
4318.30 ± 0.78	4315	4328	0.038 ± 0.005	0.17 ± 0.02	2.31	0.58	[FeII]	Opt21F
							FeII	Opt32
4346.42 ± 0.38	4285	4412	2.616 ± 0.017	12.62 ± 0.08	20.32	0.12	H γ	4341.68
4363.85 ± 0.68	4352	4372	0.110 ± 0.007	0.46 ± 0.03	3.10	−0.18	[OIII]	4364.44
4478.22 ± 1.13	4469	4484	0.029 ± 0.006	0.14 ± 0.03	2.20	−0.69	FeII	Opt37
							HeI:	4472.76
4564.71 ± 1.56	4435	4762	3.757 ± 0.029	19.52 ± 0.15	61.69[c]	0.23	FeII	Opt37
							FeII	Opt38
4686.66 ± 1.04	4668	4696	0.139 ± 0.009	0.72 ± 0.05	5.92	−0.57	HeII	4687.02
4853.13 ± 0.41	4760	4980	8.649 ± 0.030	46.21 ± 0.16	40.44	0.61	H β	4862.68
4930.75 ± 1.13	4920	4941	0.082 ± 0.007	0.40 ± 0.04	3.98	−0.02	FeII	Opt42
4960.36 ± 0.22	4945	4972	0.686 ± 0.014	3.50 ± 0.07	3.85	−0.22	[OIII]	4960.30

Table 2—Continued

λ_{obs} (Å)	λ_{lo} (Å)	λ_{hi} (Å)	Rel. Flux $100\times F/F(\mathrm{Ly}\alpha)$	W (Å)	Width σ_λ(Å)	Skew	ID[a]	λ_{lab} (Å) or Multiplet[b]
5008.22 ± 0.17	4982	5035	2.490 ± 0.031	13.23 ± 0.16	6.04	−0.22	[OIII]	5008.24
5305.97 ± 1.99	5100	5477	3.522 ± 0.036	21.47 ± 0.22	74.83[c]	−0.25	FeII	Opt48
							FeII	Opt49
5160.81 ± 0.94	5149	5168	0.092 ± 0.008	0.52 ± 0.04	3.95	−0.42	[FeVII]	5160.33
5178.68 ± 0.93	5170	5187	0.056 ± 0.007	0.32 ± 0.04	2.97	−0.23	[FeVI]	5177.48
5201.06 ± 0.98	5187	5211	0.098 ± 0.008	0.56 ± 0.05	4.42	−0.37	[NI]	5200.53
5277.92 ± 2.96	5273	5287	0.025 ± 0.007	0.14 ± 0.04	2.84	0.38	[FeVII]	5277.85
							FeII	Opt49
5313.82 ± 1.85	5302	5328	0.118 ± 0.010	0.66 ± 0.06	5.34	0.18	[FeXIV]:	5304.34
							[CaV]	5310.59
							FeII	Opt48
							FeII	Opt49
5545.16 ± 4.03	5490	5592	0.333 ± 0.021	2.12 ± 0.13	21.09	−0.04	[ClIII]:	5539.43
							FeII	Opt55
5723.74 ± 1.94	5704	5745	0.109 ± 0.015	0.70 ± 0.09	5.19	0.72	[FeVII]	5722.30
5877.41 ± 0.81	5805	5956	0.798 ± 0.029	4.94 ± 0.18	23.45	0.26	HeI	5877.29
6085.90 ± 2.00	6064	6107	0.113 ± 0.016	0.71 ± 0.10	3.78	−0.95	[FeVII]	6087.98
6303.05 ± 0.53	6283	6326	0.179 ± 0.016	1.15 ± 0.11	3.14	−0.64	[OI]	6302.05
6370.46 ± 2.67	6347	6400	0.217 ± 0.018	1.36 ± 0.11	10.18	−0.09	[OI]	6365.54
							[FeX]	6376.30
6551.06 ± 1.24	6544	6556	0.195 ± 0.029	0.43 ± 0.06	2.21	−0.20	[NII]	6549.85
6564.93 ± 0.22	6400	6765	30.832 ± 0.098	194.52 ± 0.62	47.39	0.35	H α	6564.61
6585.64 ± 0.34	6577	6593	0.831 ± 0.034	2.02 ± 0.08	2.65	−0.02	[NII]	6585.28
6718.85 ± 0.46	6708	6726	0.276 ± 0.014	1.65 ± 0.08	3.09	−0.27	[SII]	6718.29
6733.72 ± 0.46	6726	6742	0.244 ± 0.013	1.49 ± 0.08	2.54	−0.11	[SII]	6732.67
7065.67 ± 2.92	7034	7105	0.451 ± 0.026	3.06 ± 0.18	15.23	0.05	HeI	7067.20
7138.73 ± 1.12	7131	7148	0.082 ± 0.013	0.57 ± 0.09	3.13	−0.01	[ArIII]	7137.80
7321.27 ± 3.55	7285	7360	0.359 ± 0.031	2.52 ± 0.22	14.26	0.30	[OII]	7321.48
7890.49 ± 3.33	7883	7897	0.096 ± 0.018	0.69 ± 0.13	2.97	0.39	[NiIII]	7892.10
							[FeXI]	7894.00

[a] Ions ending with a colon (:) are uncertain identifications.

[b] Multiplet designations for Fe are from Netzer & Wills (1983); Grandi (1981); Phillips (1978).

[c] Broad feature composed mainly of FeII multiplets.

Table 3. Composite Quasar Absorption Line Features

λ_{obs} (Å)	W (Å)	Width σ_λ(Å)	ID	λ_{lab} (Å)
Median Composite Using All Spectra				
3800.38 ± 1.09	0.35 ± 0.03	4.14	H 10	3798.98
3837.12 ± 1.49	0.46 ± 0.03	5.96	H 9	3836.47
3934.96 ± 0.55	0.91 ± 0.03	7.11	Ca II	3934.78
8502.80 ± 7.22	1.11 ± 0.61	3.85	Ca II	8500.36
8544.17 ± 1.89	2.22 ± 0.44	3.87	Ca II	8544.44
Low-Redshift Median Composite ($z_{em} \leq 0.5$)				
3737.82 ± 1.03	0.16 ± 0.03	0.97	H 13:	3735.43
3749.45 ± 1.13	0.31 ± 0.04	2.96	H 12:	3751.22
3774.09 ± 1.27	0.36 ± 0.04	3.56	H 11	3771.70
3799.71 ± 0.89	0.84 ± 0.05	4.86	H 10	3798.98
3837.77 ± 1.16	0.95 ± 0.05	5.69	H 9	3836.47
3934.94 ± 0.48	1.64 ± 0.06	6.94	Ca II	3934.78
3974.66 ± 0.88	0.36 ± 0.04	2.42	Ca II[a]	3969.59
5892.66 ± 1.24	0.44 ± 0.05	3.72	Na II	5891.58
				5897.56
8502.80 ± 7.22	1.11 ± 0.61	3.85	Ca II	8500.36
8544.17 ± 1.89	2.22 ± 0.44	3.87	Ca II	8544.44

[a]Contaminated by emssion from [Ne III]λ3967 and H ϵ.

Table 4. Emission line velocity shifts relative to [O III]λ5007

Ion	λ_{lab} (Å)	λ_{obs} (Å)	$\Delta\lambda$ (Å)	Velocity (km/s)	Ionization Energy (eV)
Lyα	1215.67	1216.25	0.58	143 ± 91	13.60
NV	1240.14	1239.85	−0.29	−70 ± 162	97.89
CIV	1549.06	1546.15	−2.91	−563 ± 27	64.49
HeII	1640.42	1637.84	−2.58	−471 ± 151	54.42
NIII]	1750.26	1748.31	−1.95	−334 ± 128	47.45
AlIII	1857.40	1856.76	−0.64	−103 ± 190	18.83
CIII]	1908.73	1907.30	−1.43	−224 ± 28	47.89
MgII	2798.75	2800.26	1.51	161 ± 10	15.04
[NeV]	3346.82	3345.39	−1.43	−128 ± 67	126.22
[NeV]	3426.84	3426.17	−0.67	−58 ± 38	126.22
[OII]	3728.48	3729.66	1.18	94 ± 14	35.12
[FeVII]	3759.99	3758.46	−1.53	−122 ± 44	125.00
[NeIII]	3869.85	3869.77	−0.08	−6 ± 19	63.46
Hδ	4102.89	4102.73	−0.16	−11 ± 48	13.60
Hγ	4341.68	4342.02	0.34	23 ± 30	13.60
[OIII]	4364.44	4364.15	−0.29	−19 ± 48	54.94
Hβ	4862.68	4862.66	−0.02	−1 ± 14	13.60
[OIII]	4960.30	4960.36	0.06	3 ± 13	54.94
[OIII]	5008.24	5008.22	−0.02	−1 ± 10	54.94
[FeVII]	5160.33	5160.81	0.48	27 ± 54	125.00
[FeVII]	5722.30	5722.27	−0.03	−1 ± 110	125.00
HeI	5877.29	5876.75	−0.54	−27 ± 56	24.59
[FeVII]	6087.98	6086.90	−1.08	−53 ± 151	125.00
[OI]	6302.05	6303.05	1.00	47 ± 25	13.62
[NII]	6549.85	6551.06	1.21	55 ± 56	29.60
Hα	6564.61	6565.22	0.61	27 ± 13	13.60
[NII]	6585.28	6585.64	0.36	16 ± 15	29.60
[SII]	6718.29	6718.85	0.56	25 ± 20	23.33
[SII]	6732.67	6733.72	1.05	46 ± 20	23.33
[ArIII]	7137.80	7138.73	0.93	39 ± 47	40.74

Table 5. Measurements of the optical power-law continuum index for quasars.

α_ν	Sample Selection	Measurement Method	Redshift Range	Median Redshift	Source
−0.44	optical and radio	composite spectrum	0.04 – 4.79	1.25	(1)
−0.93	optical	average value from spectra	3.58 – 4.49	3.74	(2)
−0.46	radio	composite spectrum	0.02 – 3.42	0.80	(3)
−0.43	radio	composite spectrum (remeasure)	0.02 – 3.42	0.80	(3), (1)
−0.39	radio	photometric estimates	0.38 – 2.75	1.22	(4)
−0.33	optical	average value from spectra	0.12 – 2.17	1.11	(5)
−0.99	optical and radio	composite spectrum	0.33 – 3.67	0.93	(6)
−1.03	optical and radio	composite spectrum (remeasure)	0.33 – 3.67	0.93	(6), (1)
−0.46	optical	photometric estimates	0.44 – 3.36	2.00	(7)
−0.32	optical	composite spectrum	NA[a]	1.3	(8)
−0.36	optical	composite spectrum (remeasure)	NA[a]	1.3	(8), (1)
−0.67	optical	composite spectrum	0.16 – 3.78	1.51	(9)
−0.70	radio	composite spectrum	NA[a]	NA[a]	(9)

[a]The value was not given in the reference nor derivable from the data.

References. — (1) This paper; (2) Schneider et al. (2001); (3) Brotherton et al. (2000); (4) Carballo et al. (1999); (5) Natali, Giallongo, Cristiani & La Franca (1998); (6) Zheng et al. (1997); (7) Francis (1996); (8) Francis et al. (1991); (9) Cristiani & Vio (1990).

REFERENCES

Appenzeller, I. & Wagner, S. J. 1991, A&A, 250, 57

Bajtlik, S., Duncan, R. C. & Ostriker, J. P. 1988, ApJ, 327, 570

Becker, R. H., White, R. L. & Helfand, D. J. 1995, ApJ, 450, 559

Blanton, M. et al. 2001, ApJ, submitted

Boroson, T. A. & Green, R. F. 1992, ApJS, 80, 109

Brotherton, M. S., Wills, B. J., Francis, P. J. & Steidel, C. C. 1994, ApJ, 430, 495

Brotherton, M. S., Wills, B. J., Steidel, C. C. & Sargent, W. L. W. 1994, ApJ, 423, 131

Brotherton, M. S., Tran, H. T., Becker, R. H., Gregg, M. D., Laurent-Muehleisen, S. L., & White, R. L. 2000, ApJ, in press (astro-ph/0008396)

Carballo, R., González-Serrano, J. I., Benn, C. R., Sánchez, S. F. & Vigotti, M. 1999, MNRAS, 306, 137

Cid Fernandes, R. J. & Terlevich, R. 1995, MNRAS, 272, 423

Corbin, M. R. 1990, ApJ, 357, 346

Corbin, M. R. 1995, ApJ, 447, 496

Corbin, M. R. 1997, ApJ, 485, 517

Cristiani, S. & Vio, R. 1990, A&A, 227, 385

Efstathiou, A., Hough, J. H., & Young, S. 1995, MNRAS, 277, 1134

Elvis, M. et al. 1994, ApJS, 95, 1

Espey, B. & Andreadis, S. 1999, ASP Conf. Ser. 162: Quasars and Cosmology, 351

Espey, B. R., Carswell, R. F., Bailey, J. A., Smith, M. G. & Ward, M. J. 1989, ApJ, 342, 666

Fan, X. et al. 1999, AJ, 118, 1

Fan, X. et al. 2000, AJ, 119, 1

Fan, X. et al. 2001, AJ, 121, 31 R. J., Peterson, B. M., Sun, L., Malkan, M. A. & Chaffee, F. H. 1986, ApJ, 307, 504

Foltz, C. B., Weymann, R. J., Peterson, B. M., Sun, L., Malkan, M. A., & Chaffee, F. H. 1986, ApJ, 307, 504

Forster, K., Green, P. J., Aldcroft, T. L., Vestergaard, M., Foltz, C. B., & Hewett, P. C. 2001, ApJS, in press (astro-ph/0011373)

Francis, P. J. 1996, Publications of the Astronomical Society of Australia, 13, 212

Francis, P. J. 1993, ApJ, 407, 519

Francis, P. J., Hewett, P. C., Foltz, C. B. & Chaffee, F. H. 1992, ApJ, 398, 476

Francis, P. J., Hewett, P. C., Foltz, C. B., Chaffee, F. H., Weymann, R. J. & Morris, S. L. 1991, ApJ, 373, 465

Frieman, J. A., et al. 2001, in preparation

Franx, M., Illingworth, G. & Heckman, T. 1989, ApJ, 344, 613

Fukugita, M., Ichikawa, T., Gunn, J. E., Doi, M., Shimasaku, K. & Schneider, D. P. 1996, AJ, 111, 1748

Gaskell, C. M. 1982, ApJ, 263, 79

Graham, M. J., Clowes, R. G. & Campusano, L. E. 1996, MNRAS, 279, 1349

Grandi, S. A. 1977, ApJ, 215, 446

Grandi, S. A. 1981, ApJ, 251, 451

Grandi, S. A. 1982, ApJ, 255, 25

Gunn, J. E. et al. 1998, AJ, 116, 3040

Heckman, T. M., Butcher, H. R., Miley, G. K. & van Breugel, W. J. M. 1981, ApJ, 247, 403

Hutchings, J. B., Gower, A. C. & Price, R. 1987, AJ, 93, 6

Kriss, G. A., Peterson, B. M., Crenshaw, D. M. & Zheng, W. 2000, ApJ, 535, 58

Laor, A., Bahcall, J. N., Jannuzi, B. T., Schneider, D. P. & Green, R. F. 1995, ApJS, 99, 1

Laor, A., Jannuzi, B. T., Green, R. F. & Boroson, T. A. 1997, ApJ, 489, 656

Lupton, R. H., 1993, Statistics in Theory and Practice, (Princeton University Press)

Mathis, J. S., Rumpl, W. & Nordsieck, K. H. 1977, ApJ, 217, 425

McIntosh, D. H., Rix, H.-W., Rieke, M. J. & Foltz, C. B. 1999, ApJ, 517, L73

McLure, R. J., Kukula, M. J., Dunlop, J. S., Baum, S. A., O'Dea, C. P., & Hughes, D. H. 1999, MNRAS, 308, 377

McLure, R. J. & Dunlop, J. S. 2000, MNRAS, 317, 249

Menou, K., et al. 2001, AJ, submitted

Mirabel, I. F. & Wilson, A. S. 1984, ApJ, 277, 92

Natali, F., Giallongo, E., Cristiani, S. & La Franca, F. 1998, AJ, 115, 397

Netzer, H. 1977, MNRAS, 181, 89

Netzer, H. & Wills, B. J. 1983, ApJ, 275, 445

Neugebauer, G., Green, R. F., Matthews, K., Schmidt, M., Soifer, B. T. & Bennett, J. 1987, ApJS, 63, 615

Newberg, H. J., et al. 2001, in preparation

Newberg, H. J., Richards, G. T., Richmond, M., & Fan, X. 1999, ApJS, 123, 377

Nolan, L. A., Dunlop, J. S., Kukula, M. J., Hughes, D. H., Boroson, T., Jimenez, R. 2001, MNRAS, submitted, (astro-ph/0002020)

Oke, J. B. & Lauer, T. R. 1979, ApJ, 230, 360

Oke, J. B., Shields, G. A. & Korycansky, D. G. 1984, ApJ, 277, 64

Osterbrock, D. E. 1981, ApJ, 246, 696

Osterbrock, D. E., Tran, H. D. & Veilleux, S. 1992, ApJ, 389, 305

Penston, M. V. 1977, MNRAS, 180, 27P

Penston, M. V., Fosbury, R. A. E., Boksenberg, A., Ward, M. J., & Wilson, A. S. 1984, MNRAS, 208, 347

Phillips, M. M. 1976, ApJ, 208, 37

Phillips, M. M. 1978, ApJS, 38, 187

Pitman, K. M., Clayton, G. C. & Gordon, K. D. 2000, PASP, 112, 537

Puget, J. L., Leger, A., & Boulanger, F. 1985, A&A, 142, L19

Richards, G. T., et al. 2001, AJ, 121, in press.

Richards, G. T., et al. 2001, in preparation

Schlegel, D. J., Finkbeiner, D. P., & Davis, M. 1998, ApJ, 500, 525

Schneider, D. P., Schmidt, M. & Gunn, J. E. 1991, AJ, 101, 2004

Schneider, D. P. et al. 2000, PASP, 112, 6

Schneider, D. P. et al. 2001, AJ, in press

Serote Roos, M., Boisson, C., Joly, M., & Ward, M. J. 1998, MNRAS, 301, 1

Siegmund, W., et al. 2001, in preparation

Snijders, M. A. J., Netzer, H. & Boksenberg, A. 1986, MNRAS, 222, 549

Stoughton, C. et al. 2001, in preparation

Tadhunter, C. N., Metz, S. & Robinson, A. 1994, MNRAS, 268, 989

Terlevich, E., Diaz, A. I., & Terlevich, R. 1990, MNRAS, 242, 271

Tytler, D. & Fan, X. 1992, ApJS, 79, 1

Uomoto, A., et al. 2001, in preparation

Vanden Berk, D. E., et al. 2001, in preparation

Verner, E. M., Verner, D. A., Korista, K. T., Ferguson, J. W., Hamann, F. & Ferland, G. J. 1999, ApJS, 120, 101

Vrtilek, J. M. & Carleton, N. P. 1985, ApJ, 294, 106

Weymann, R. J., Morris, S. L., Foltz, C. B. & Hewett, P. C. 1991, ApJ, 373, 23

Whittle, M. 1985, MNRAS, 216, 817

Wilkes, B. J. 1986, MNRAS, 218, 331

Wills, B. J., Laor, A., Brotherton, M. S., Wills, D., Wilkes, B. J., Ferland, G. J. & Shang, Z. 1999, ApJ, 515, L53

Wills, B. J., Netzer, H. & Wills, D. 1985, ApJ, 288, 94

York, D. G. et al. 2000, AJ, 120, 1579

Zheng, W., Kriss, G. A., Telfer, R. C., Grimes, J. P. & Davidsen, A. F. 1997, ApJ, 475, 469

Zheng, W. et al. 2000, AJ, 120, 1607

Zheng, W. & Sulentic, J. W. 1990, ApJ, 350, 512

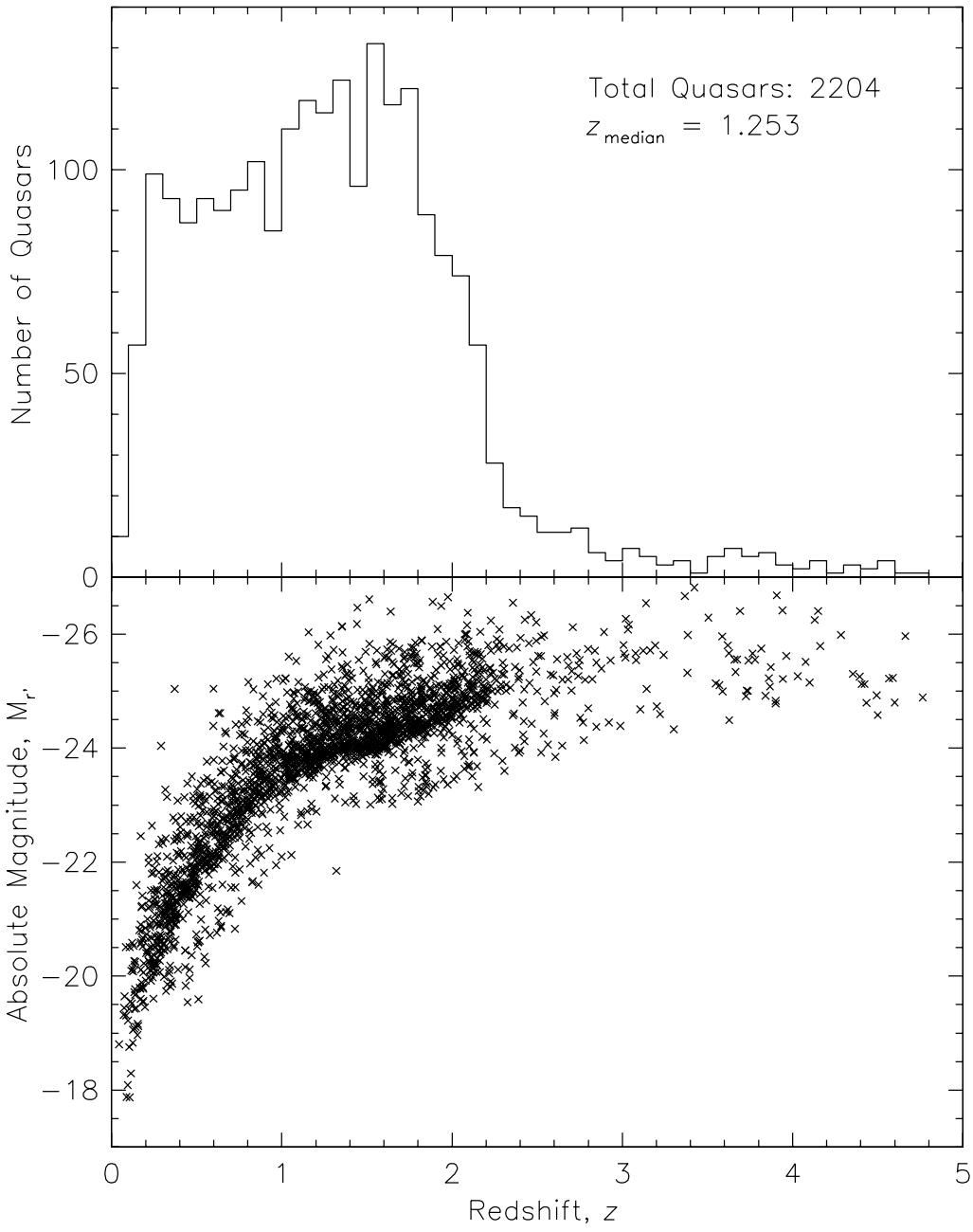

Fig. 1.— Redshift distribution of the 2204 quasars used for the composite spectra (top), and the absolute r' magnitude, $M_{r'}$, vs. redshift (bottom). The median redshift is $z = 1.253$.

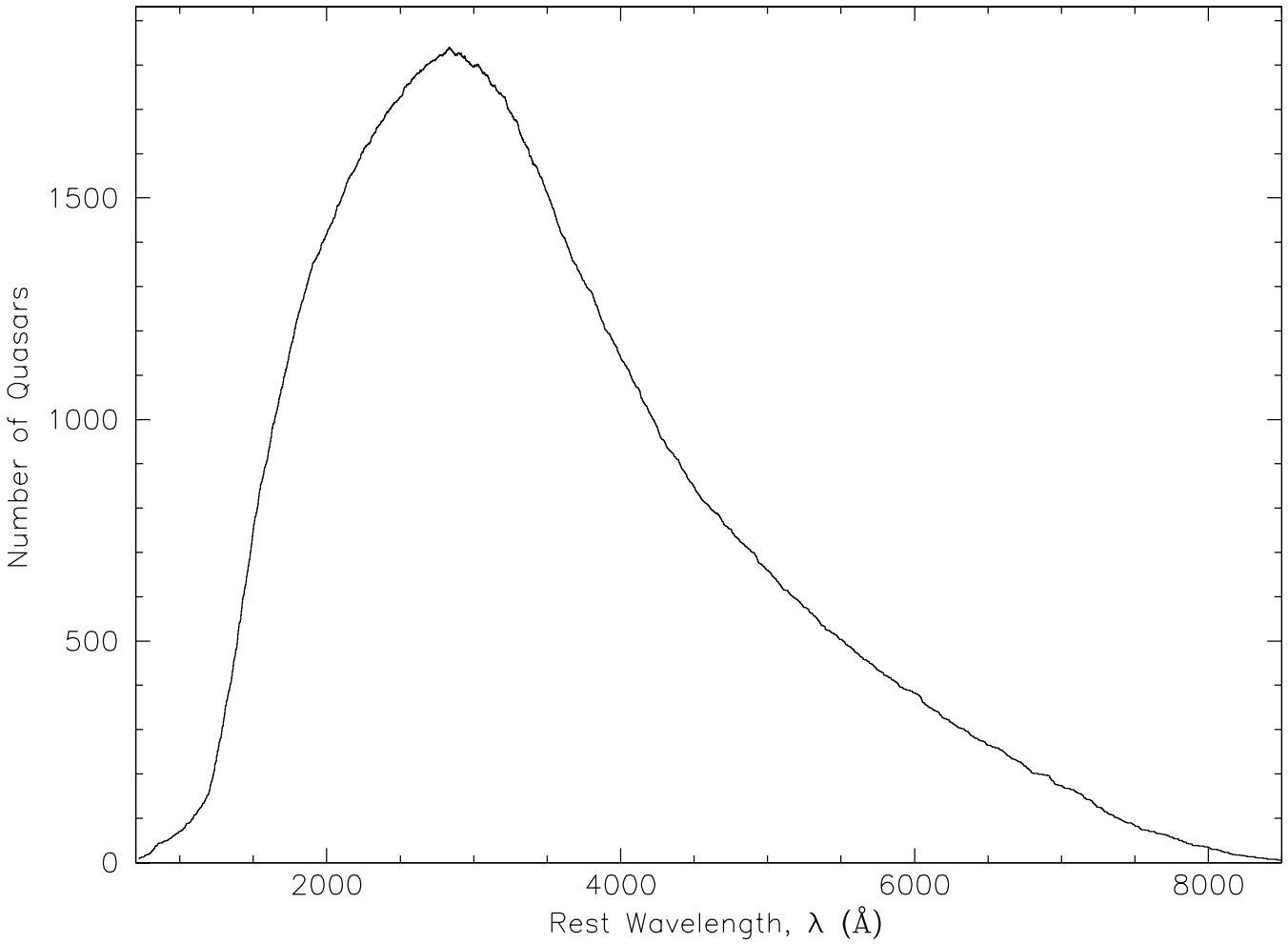

Fig. 2.— Number of quasar spectra combined in each 1 Å bin of the composite as a function of rest wavelength.

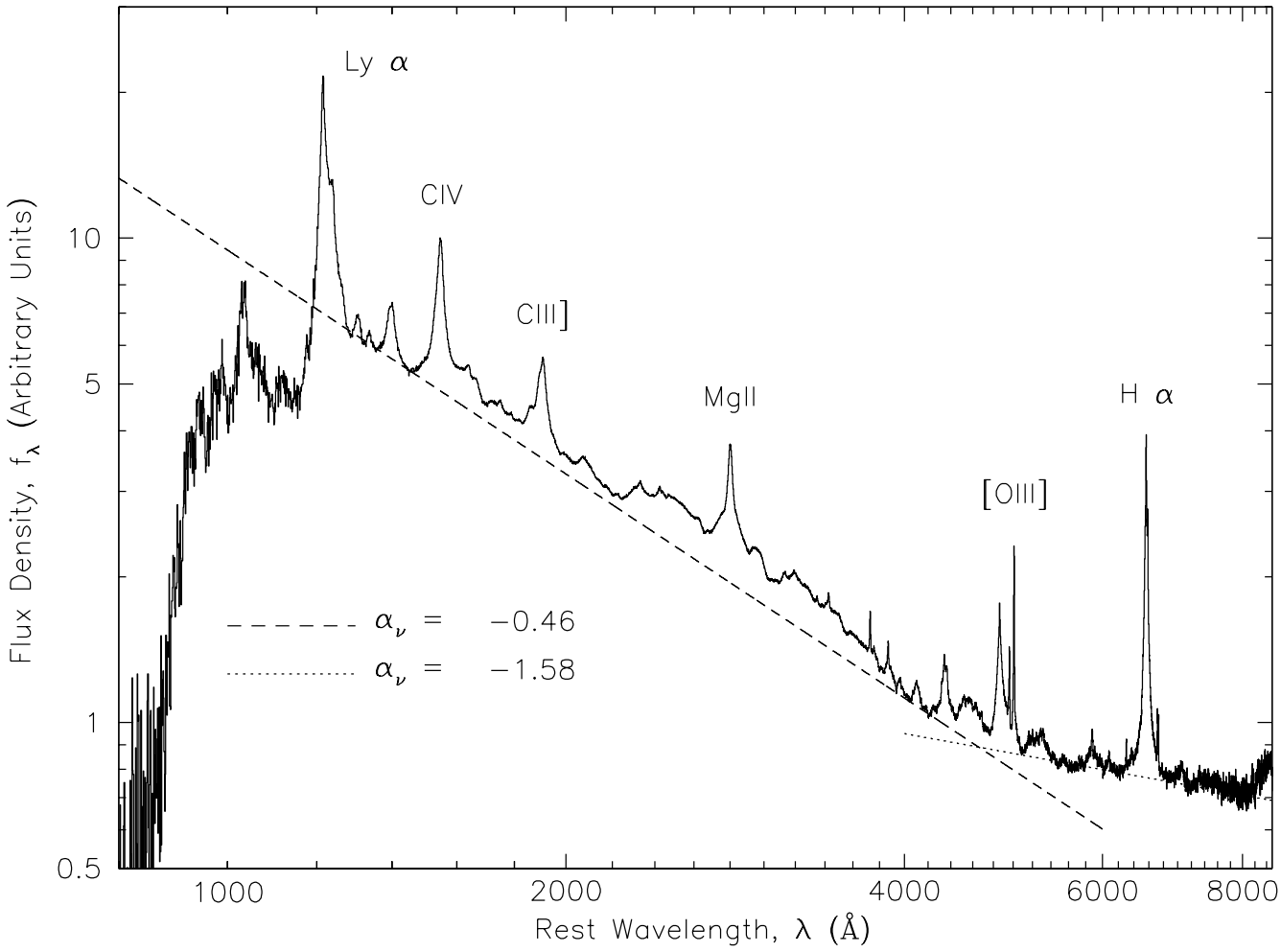

Fig. 3.— Composite quasar spectrum using median combining. Power-law fits to the estimated continuum flux are shown. The resolution of the input spectra is ≈ 1800, which gives a wavelength resolution of about 1Å in the rest frame.

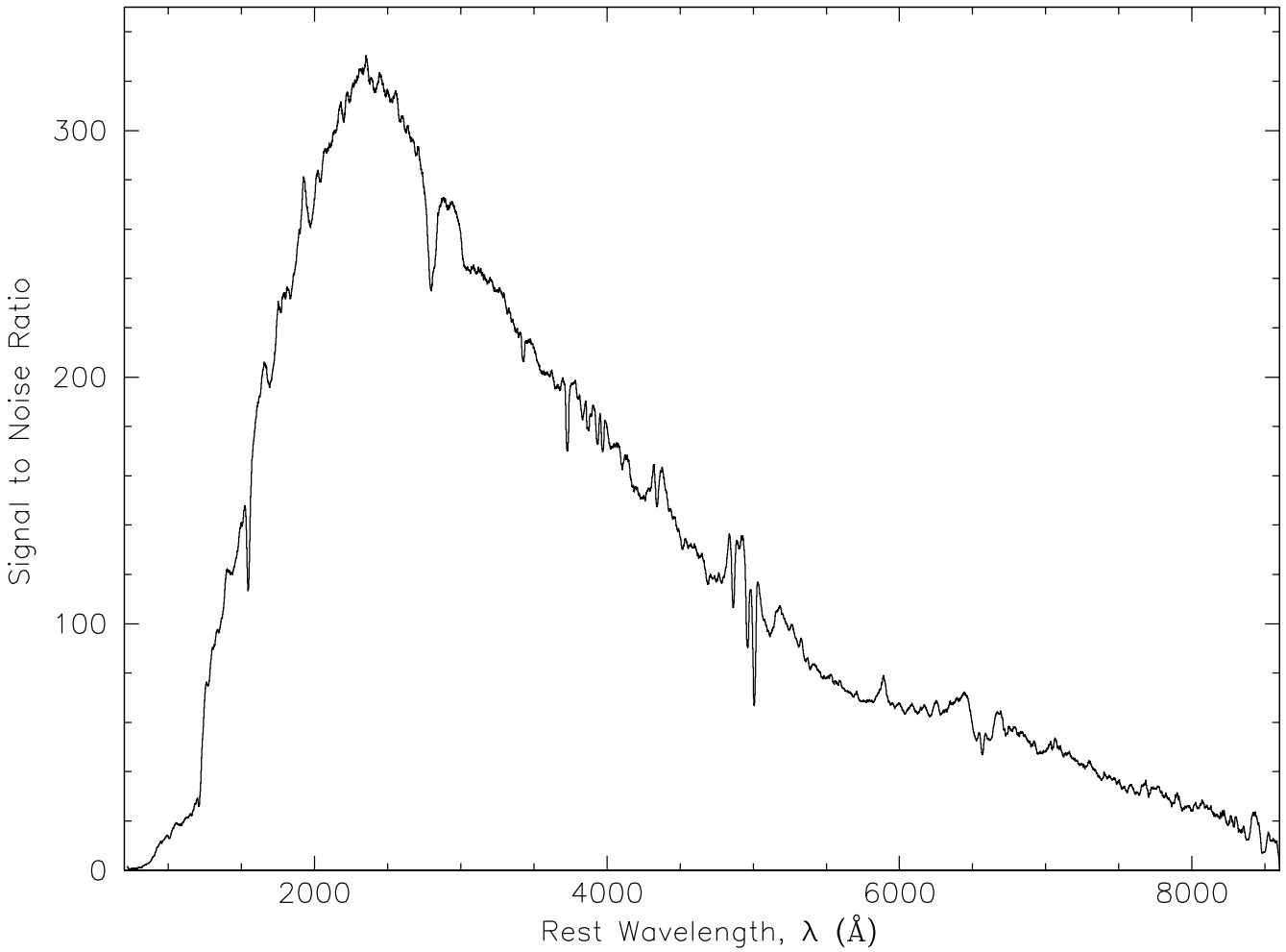

Fig. 4.— Signal to noise ratio per 1Å bin for the median composite quasar spectrum. The peak reaches almost 330 at 2800 Å.

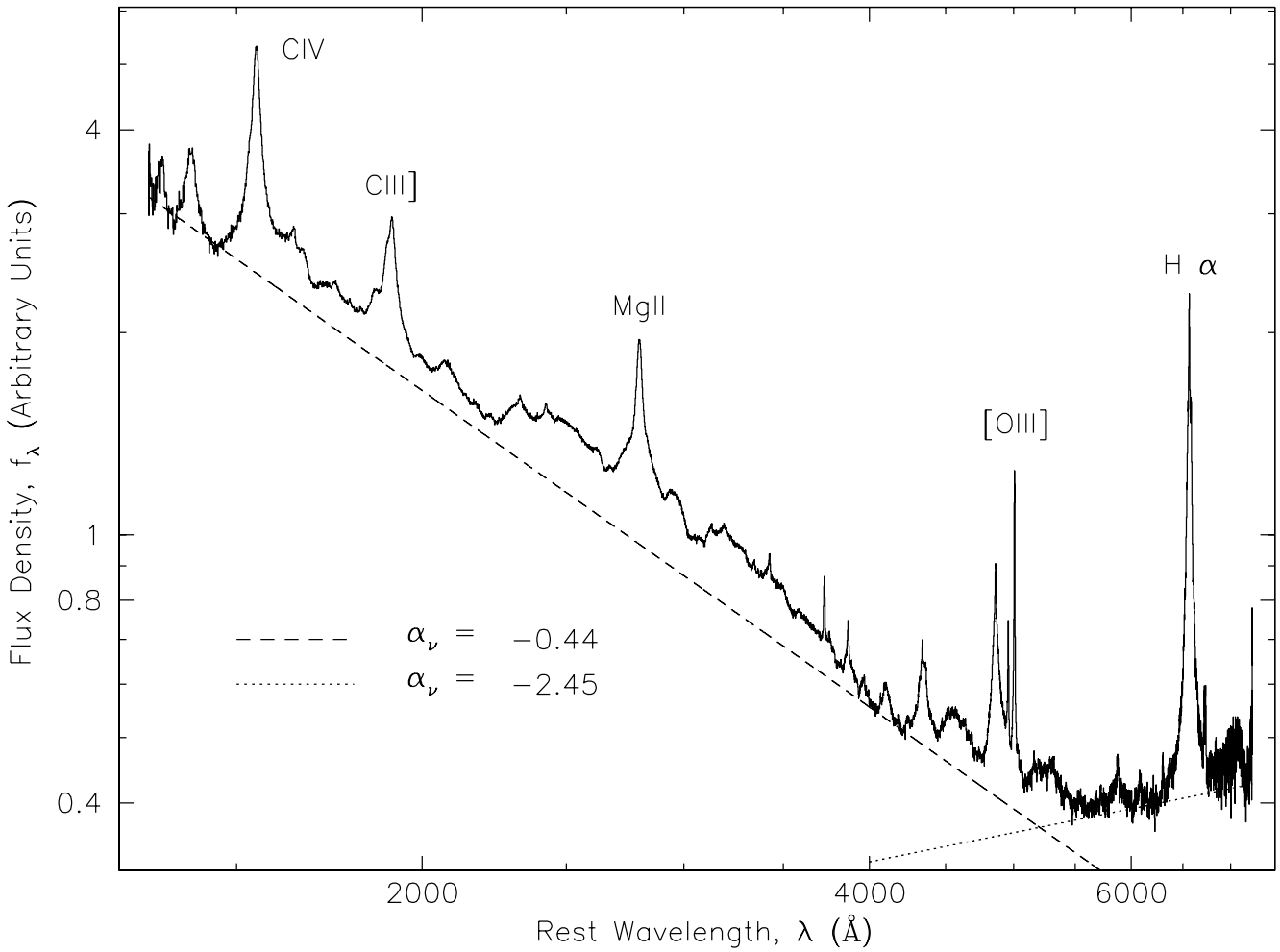

Fig. 5.— Composite quasar spectrum generated using the geometric mean of the input spectra. Power-law fits to the estimated continuum flux are shown. The geometric mean is a better estimator than the arithmetic mean (or median) for power-law distributions. The resolution of the input spectra is ≈ 1800 in the observed frame, which gives a wavelength resolution of about 1Å in the rest frame.

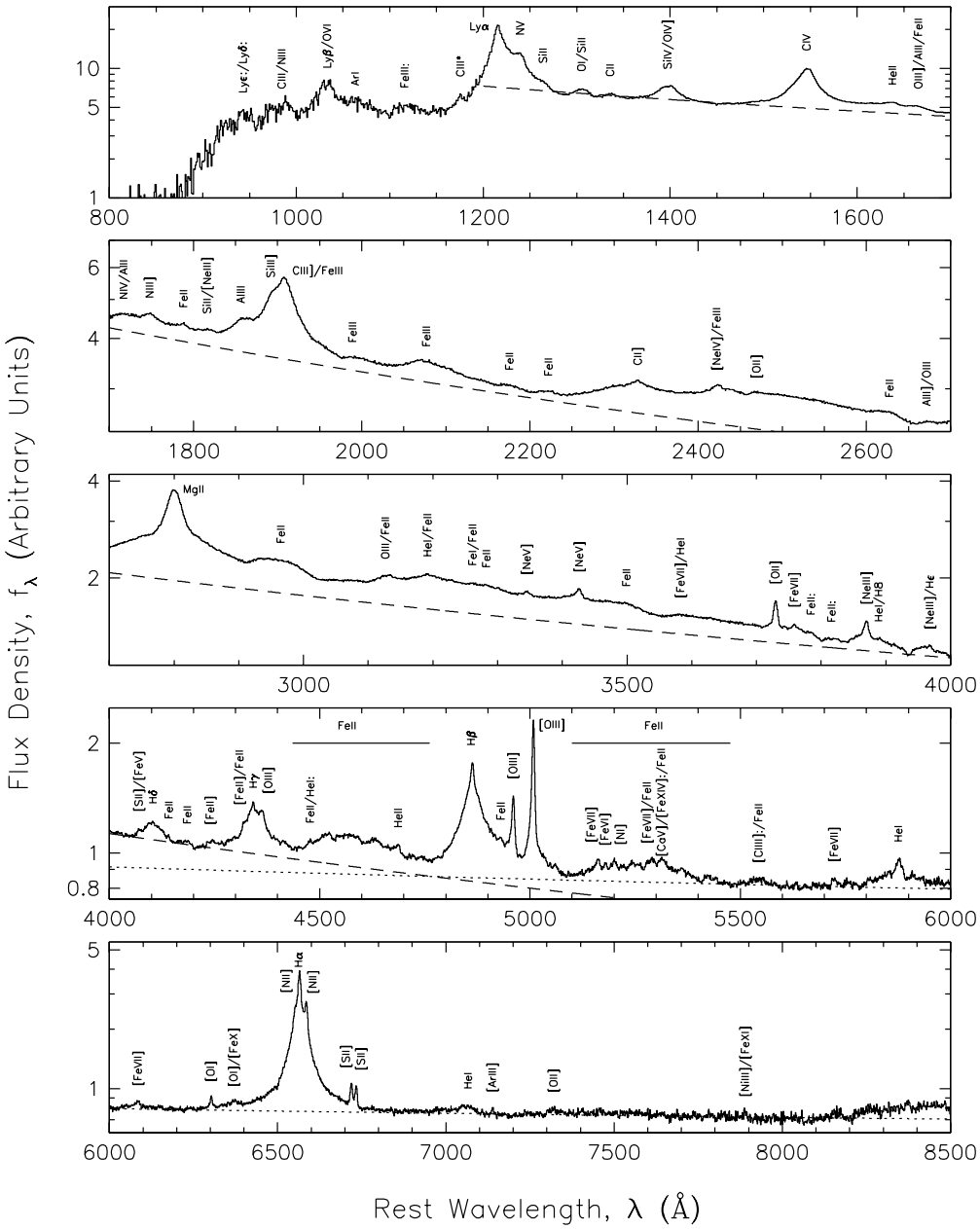

Fig. 6.— Expanded view of median quasar composite on log-linear scale, with emission features labeled by ion. Labels ending with a colon (:) are uncertain identifications. The two power-law continuum fits are shown by dashed and dotted lines. The flux from 1600-3800 Å is also composed of heavily blended Fe II and Fe III lines, and Balmer continuum emission.

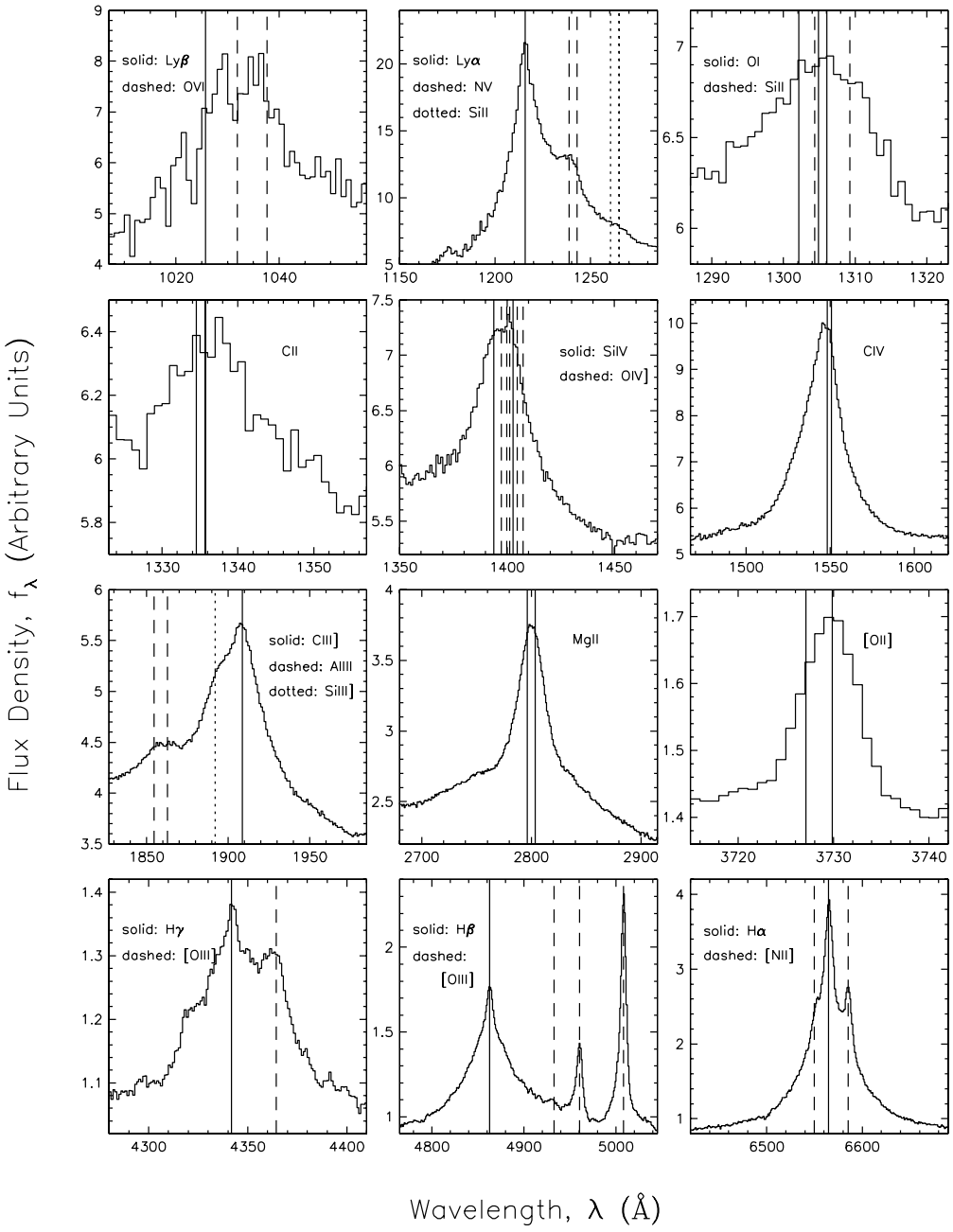

Fig. 7.— Detailed view of 12 strong emission line regions. The laboratory rest wavelength positions of the major line components are shown. Many of the emission lines are composed of blended multiple transitions (doublets, triplets, etc.) from the same ion.

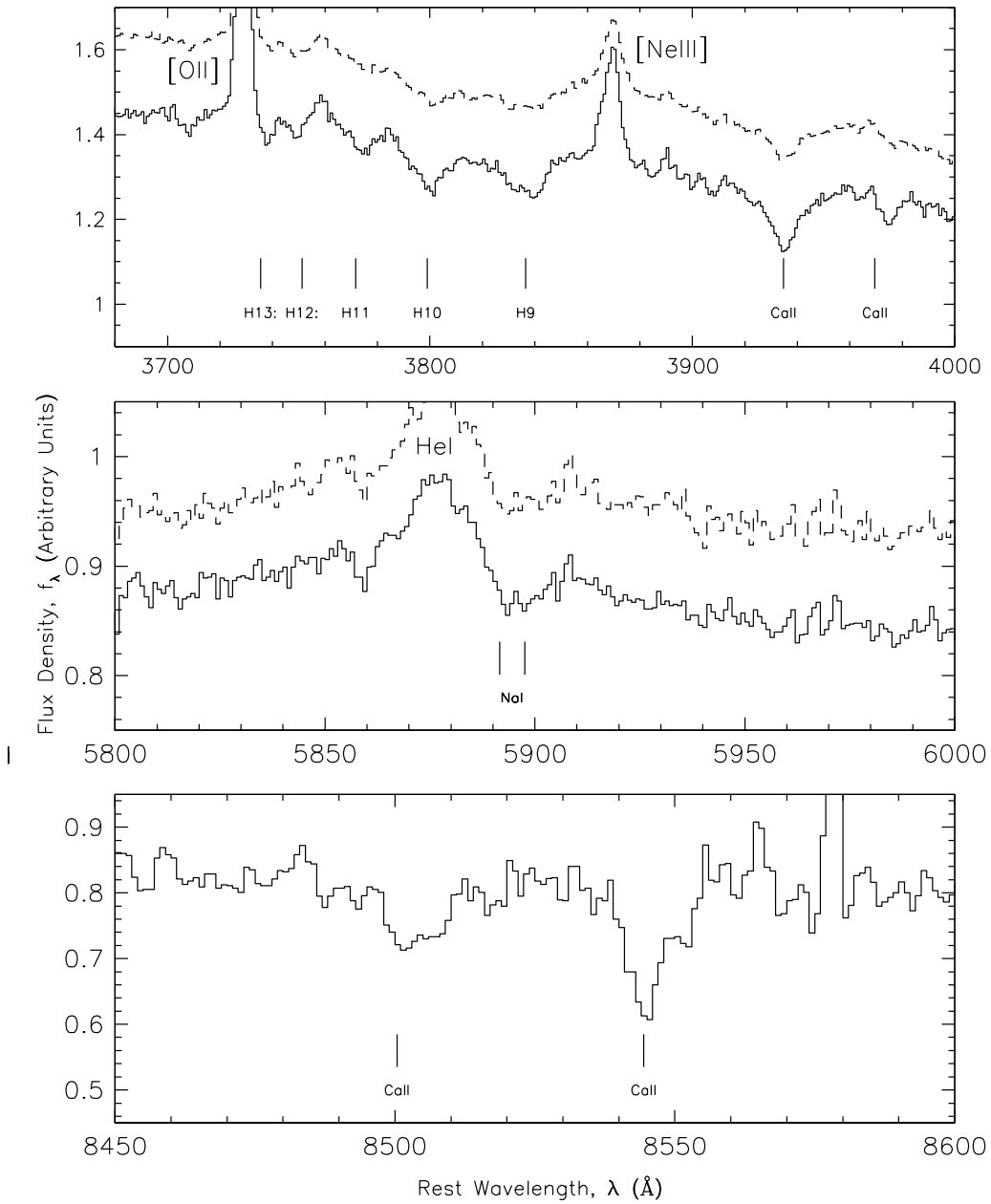

Fig. 8.— Detailed view of absorption line regions in the low-redshift composite quasar spectrum (solid line). The laboratory rest wavelength positions of detected absorption lines are labeled by ion. Several strong emission lines are also labeled. The Ca IIλ3968 line is contaminated by emission from [Ne III]λ3967 and Hϵ. The full-sample composite spectrum (dashed line, offset) is also shown for comparison in the top two panels (the spectra are identical in the wavelength region covered in the bottom panel).

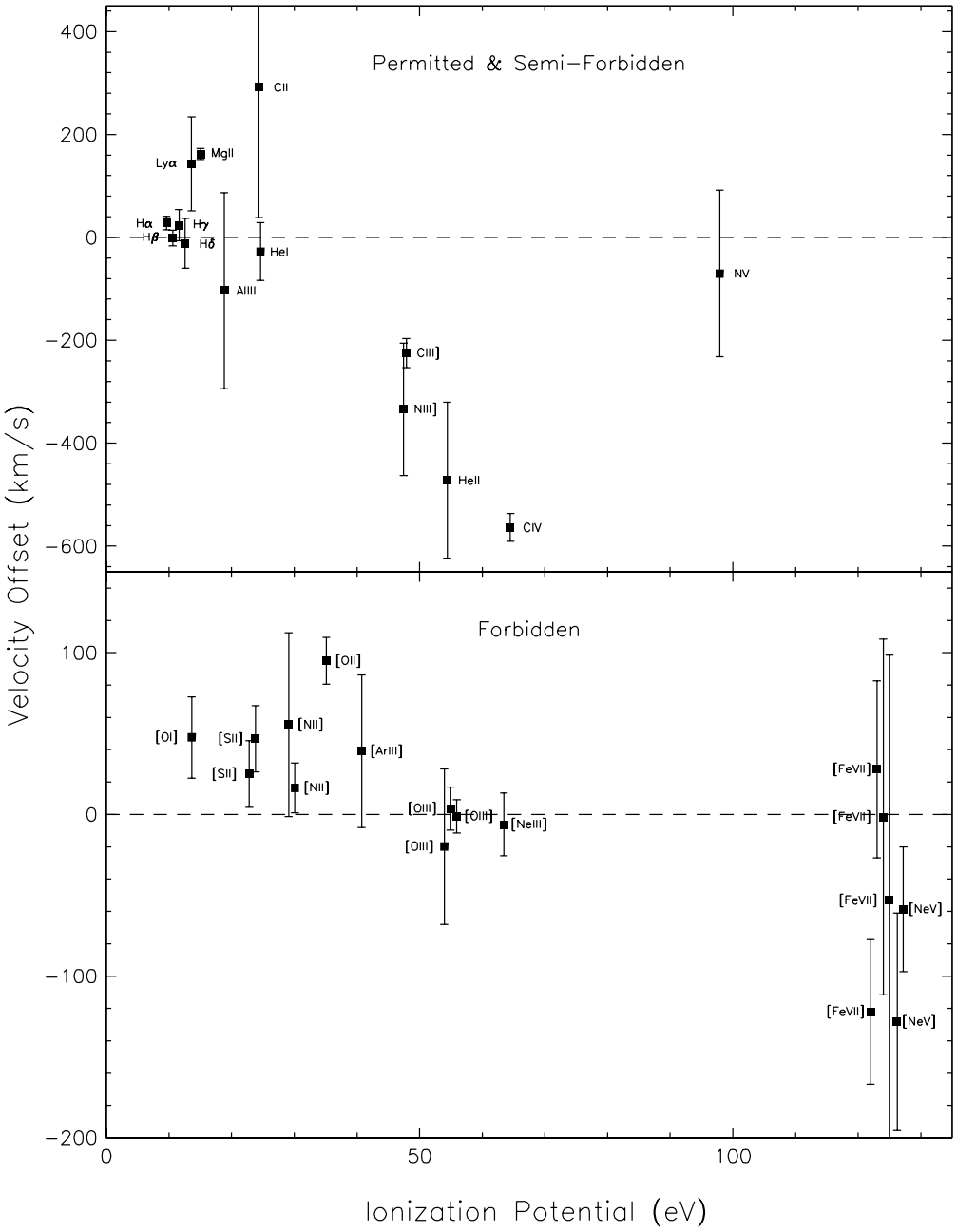

Fig. 9.— Emission line velocity offsets relative to laboratory rest wavelengths as a function of ionization potential for selected emission lines. Error bars show the 1 standard deviation uncertainty in the velocity measurement. The points are labeled by ion. Ionization potentials corresponding to the same ion are slightly offset from each other for clarity. Permitted and semi-forbidden lines are shown in the top panel, and forbidden lines are shown in the bottom panel.

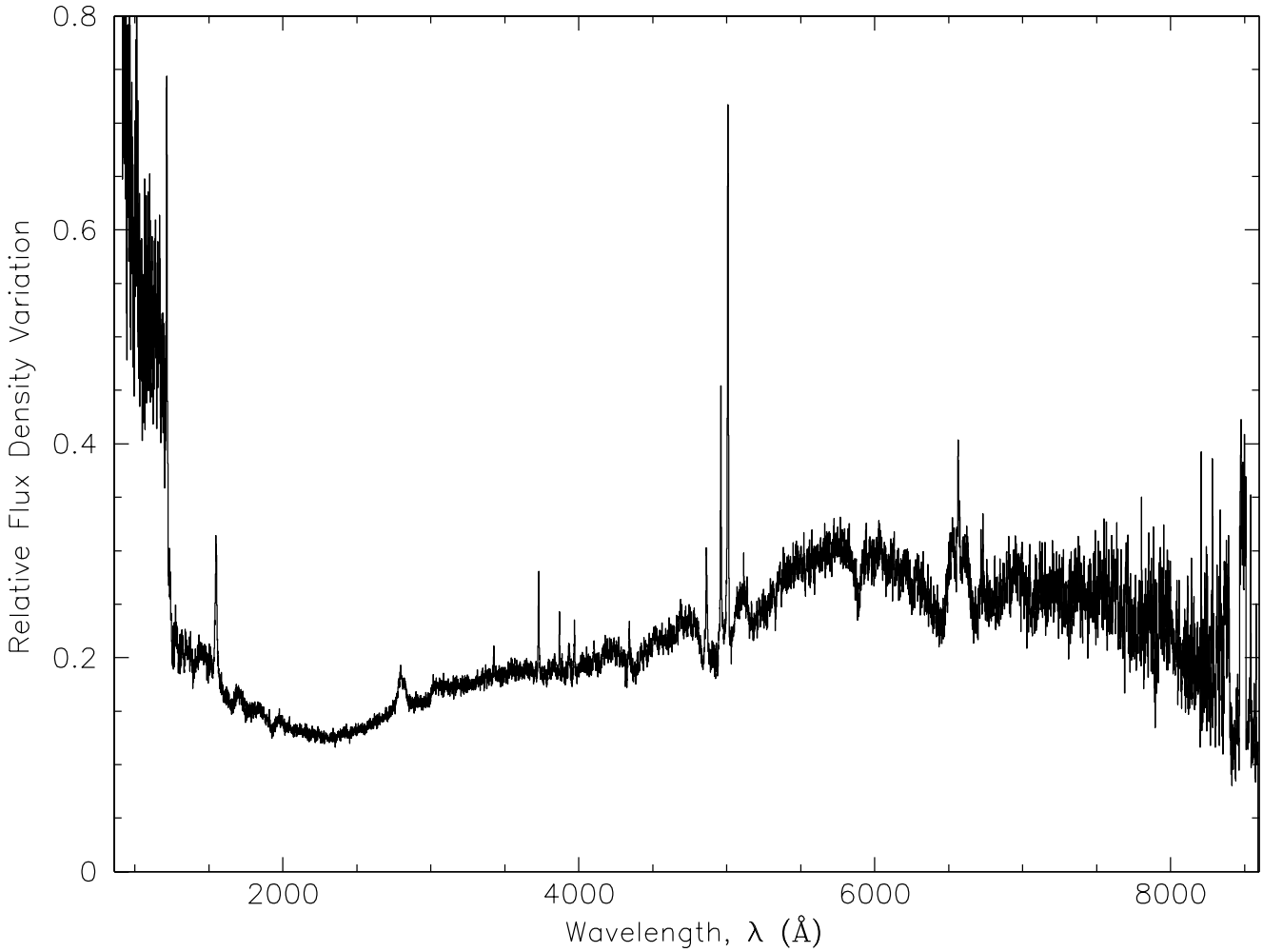

Fig. 10.— Spectrum-to-spectrum variation of the quasar composite flux density relative to the median flux as a function of rest wavelength.

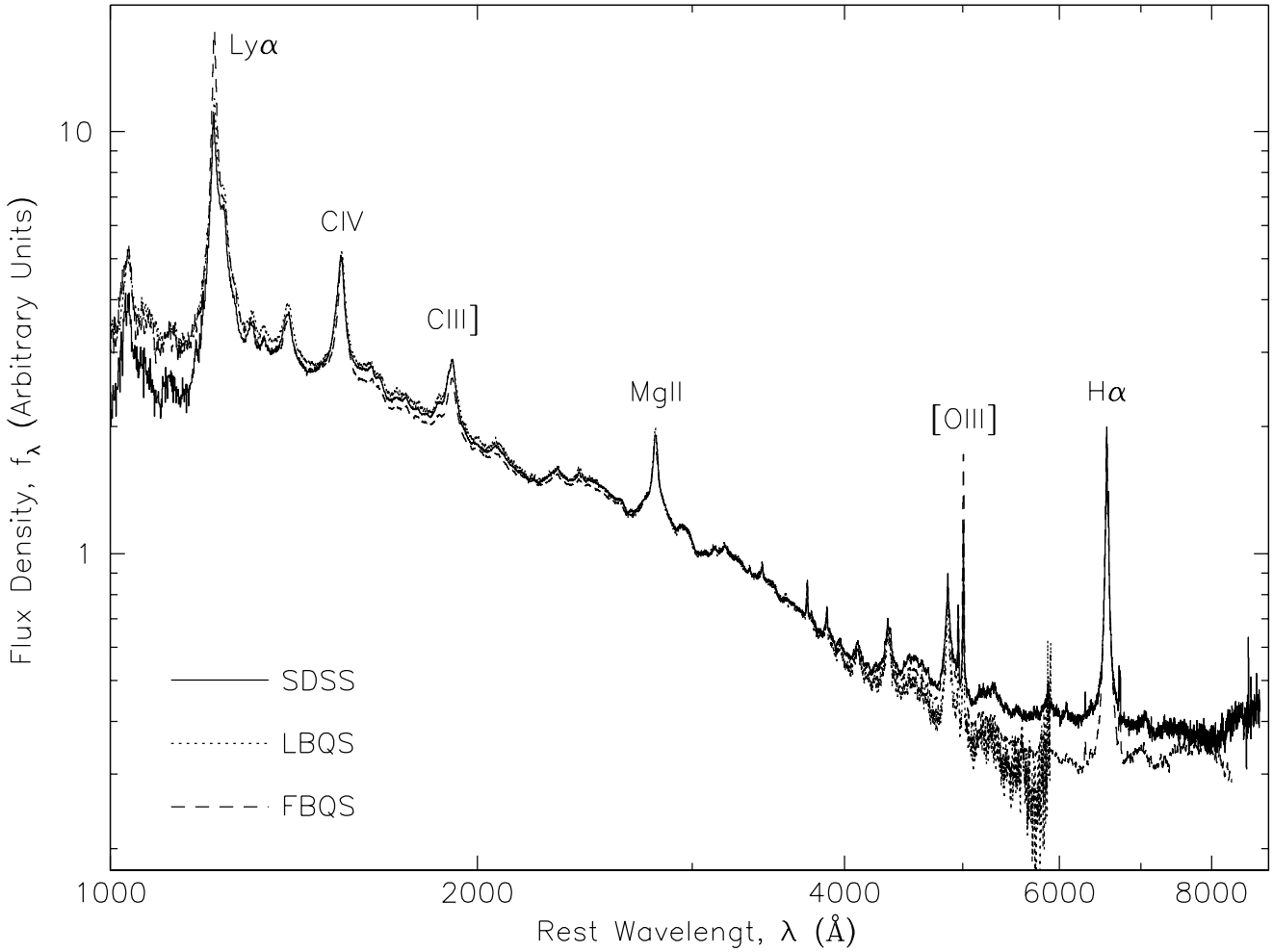

Fig. 11.— Comparison of the SDSS median quasar composite spectrum (solid) with the LBQS (dotted) and FBQS (dashed) composites. The spectra are scaled to the same average flux density between 3020 and 3100Å. Several major emission lines are labeled for reference.